

From the Editorial Committee

Dear Reader

It is our pleasant privilege to forward a copy of the latest issue of IGC Newsletter (Volume 125, July 2020 issue).

In the first technical article, Dr. Chinnappan Ravi of Materials Science Group has discussed about the “Energetics of Point Defects in BCC Ferromagnetic Iron-Computation using Density Functional Theory”.

In the second technical article, Dr. K. C. Pitchaiah and colleagues, Materials Chemistry & Metal Fuel Cycle Group have discussed about the “Recovery of Actinides using Supercritical Fluid Extraction: A Green Separation Technique”.

Shri G. Vikram, Reactor Design and Technology Group has described about the “Plant Dynamics Modeling of Inadvertent Closure of Sodium Side Isolation Valve of a Single SG in a SFR” in the Young Officer’s Forum.

This issue’s Young Researcher’s Forum features an article by Shri Surojit Ranoo, Metallurgy & Materials Group, IGCAR discussing about “A Novel Approach to Enhance Magnetic Field Induced Heating Efficiency in Magnetic Fluids Through in-situ Orientation”.

We are happy to share with you the awards, honours and distinctions earned by our colleagues.

We look forward to your comments, continued guidance and support.

With best wishes and personal regards

Editorial Committee, IGC Newsletter

Energetics of Point Defects in BCC Ferromagnetic Iron-Computation using Density Functional Theory

Ferritic and Martensitic stainless steels offer better dimensional stability than austenitic steels under neutron irradiation in fast spectrum reactors. The operating temperatures of these steels are however limited to about 560°C. To achieve higher operating temperatures, oxide dispersion strengthened (ODS) steels have been developed for fuel clad and wrapper core components. These modern steels are multicomponent alloys with about 20 components (Fe, C, Mn, P, Si, Ni, Cr, Mo, V, Ti, Co, Cu, Al, B, W, Zr, N and Y). These steels are made up of Fe-Cr ferritic matrix with a homogeneous distribution of precipitates created by ball milling and subsequent consolidation through hot extrusion or isostatic pressing. These steels have superior creep resistance and stability under irradiation, attributed to the densely dispersed finest oxide precipitates in the ferritic matrix with high dislocation density. These nano-precipitates are very stable even up to the solidus of the steel.

Stability of the microstructure of these steels under irradiation is also important for their long-term service in the nuclear environment. The evolution of size and population of the nanoparticles is not however well understood. Formation and binding energies of the point defects profoundly influence the diffusion of solutes and hence nucleation, growth and coarsening of precipitates. For instance, the unusually high solubility of oxygen atoms and nucleation of stable oxygen enriched nanoparticles in iron is determined by the formation and binding energies of vacancy, oxygen and other solutes present in it. Modelling of clustering of atomic defects and swelling in iron also suggests that accurate characterization of the interactions of the solutes with the other point defects is important. Further, the addition of tin solutes at the ppm level in Al-Mg-Si alloys have been found to inhibit natural aging and enhance artificial aging. The mechanism of controlling the aging is vacancy diffusion, with solutes trapping vacancies at low temperatures and releasing them at elevated temperatures. This “diffusion on demand” solves the long-standing problem of the detrimental natural aging in Al-Mg-Si alloys, which is of great scientific and industrial importance. Moreover, the mechanism of controlled buffering and release of excess vacancies is generally applicable to modulate diffusion in other metallic systems.

Density Functional Theory (DFT) calculations have emerged, on the other hand, as a powerful approach to study the thermodynamic and kinetic properties of point defects and hence to develop an atomic level understanding of their interactions in solids. Therefore, an extensive set of DFT calculations have been performed for the formation and binding energies of point defects in ferromagnetic body centred cubic (bcc) iron for an extended set of solute elements, M, with atomic numbers from 1 to 54, modelled with Fe_{53}M_1 and $\text{Fe}_{52}\text{M}_1\text{V}_1$ systems (V represents a vacancy) based on a $3 \times 3 \times 3$ bcc supercell of 54 lattice sites. Figure 1 illustrates the supercell model of bcc iron with point defects. In the Figure, labels 1, 2 and 3 represent substitutional sites. Labels 4 to 12 represent octahedral interstitial sites. Solute-solute nearest neighbour pair configuration was obtained by substituting the Fe atoms at sites 1 and 2 with the given solute atoms. Vacancy-solute first and second neighbour pairs were formed by placing the given solute atom at site 2 or 3 respectively, while site 1 is made vacant. A single interstitial atom defect was formed by placing the atom

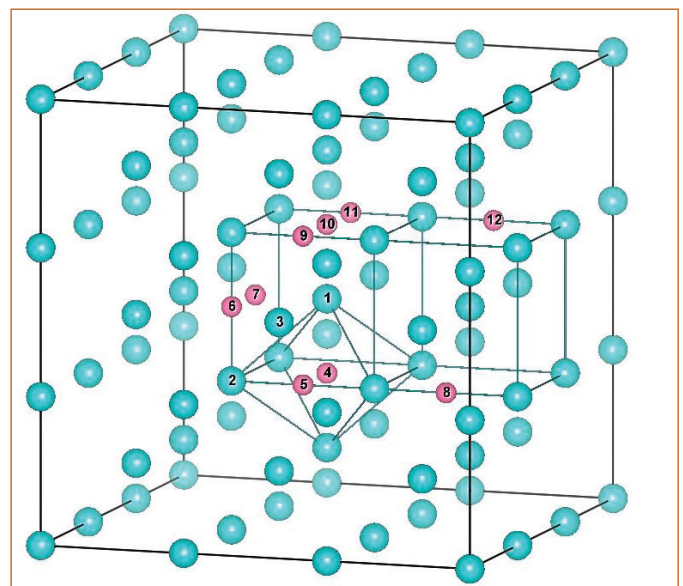


Figure 1: BCC $3 \times 3 \times 3$ supercells with labelled atoms to define atomic defect configurations. Pairs of interstitial atoms were created by placing them at pairs of sites 5-6, 5-7, 5-8, 5-9, 5-10, 5-11 and 5-12, respectively. Vacancy-interstitial pairs were formed by removing the atom at site 1 and placing an interstitial atom at site 4 or 5 respectively for 1st and 2nd neighbour configurations

at site 4. The results are then analyzed to identify physical trends in the formation and binding energies of the solutes in bcc iron. We note here that although the alkali metals and noble gas atoms do not generally alloy with iron, knowledge of their energetics in iron matrix will be useful to see trends in the solution behaviour of atoms in iron. Further, nuclear fission products include elements from alkaline earth, alkali, halogen and noble gas elements. For modelling interaction of these fission products with steel cladding as well as for modelling nuclide distribution between steelmaking phases upon melting of sealed radioactive sources hidden in scrap, knowledge of their formation energies are useful. Furthermore, oxygen and yttrium atoms are practically immiscible in Fe but ODS steels with clusters of these elements are produced through mechanical alloying. Similarly, ion beam mixing is used to mix immiscible Ag, In and Na in iron. Ion implantation is used for similar synthesis. For modelling such alloying approaches, energetics of these solutes will be useful. Further the interactions of self interstitial atom defects with vacancies and solute elements are also important for a robust understanding of atomic transport in steels. In this work, however self-interstitial atom defects are not considered

The formation energy, E_f^M , of a substitutional solute M was calculated from:

$$E_f^M = E(\text{Fe}_{N-1}\text{M}_1) - \frac{[N - (1 + \frac{m}{n})]}{N} E(\text{Fe}_N) - \frac{1}{n} E(\text{Fe}_m\text{M}_n) \quad (1)$$

where $E(\text{Fe}_{N-1}\text{M}_1)$ is the total energy of the iron supercell with N lattice sites containing a solute M and (N-1) Fe atoms. Fe_mM_n

is the reference phase in our calculation of the solute formation energies. It is the second phase with which the solid solution phase is in equilibrium. It can be a compound phase, elemental crystal, molecules or atoms. In Fe_mM_n , m and n are integers specifying the stoichiometry. The binding energy, E_b^{M-M} , of a substitutional solute-solute (M-M) pair configuration was calculated using:

$$E_b^{M-M} = [E(\text{Fe}_{N-2}\text{M}_2) + E(\text{Fe}_N)] - 2[E(\text{Fe}_{N-1}\text{M}_1)] \quad (2)$$

where $E(\text{Fe}_{N-2}\text{M}_2)$ is the total energy of the iron supercell with N sites containing a pair of substitutional solutes M and (N-2) Fe atoms. Similar expressions were used for the formation and binding energies involving interstitial solutes. The total energy calculations were performed using the Vienna Ab initio Simulation Package.

Solute Formation Energies, Solubility and Size Factors

Solute formation energies are useful to understand the solid state solubility and alloying behaviour. The solubility predicted by our solute formation energies are generally in agreement with those obtained from phase diagrams. Figure 2 displays the formation energies of solute atoms M in bcc Fe. We see that the formation energies of solute elements from fourth and fifth periods vary with their atomic numbers such that they reach maxima near the ends of the periods and minima in between, with a local hump near Cu and Ag (like a quasiparabolic valley). Solute elements from second and third periods show a similar trend to the elements near the ends

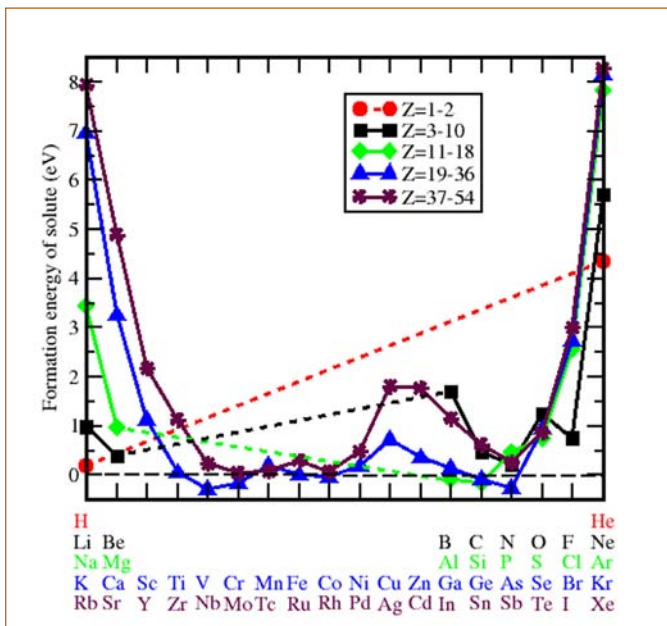


Figure 2: Formation energies of solute atoms M in bcc Fe

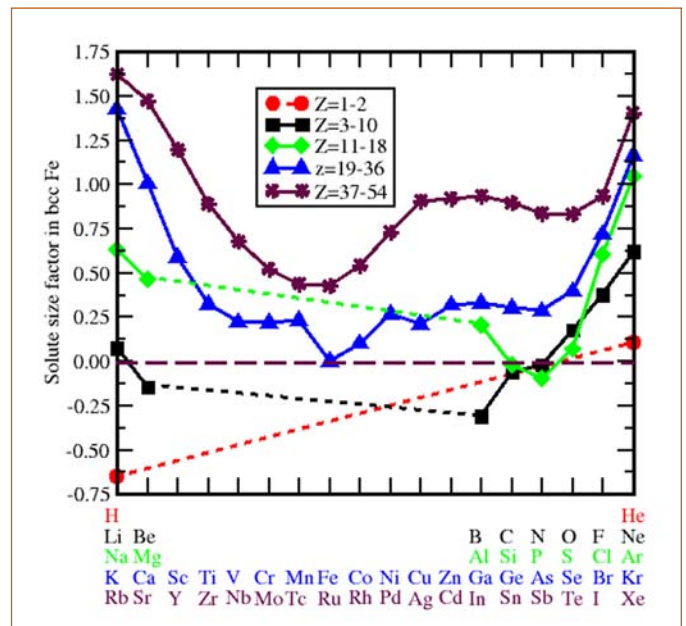


Figure 3: The size factors of the solute atoms M in bcc Fe

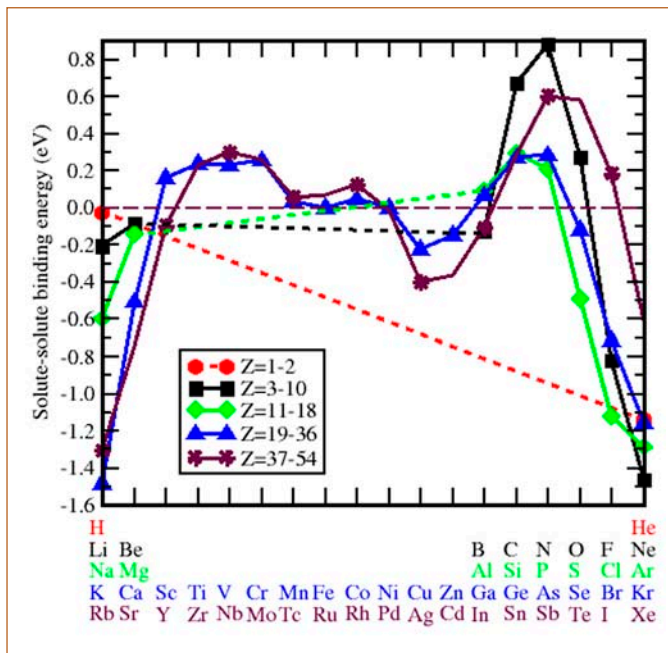


Figure 4: Solute-solute binding energies in bcc Fe

of the fourth and fifth periods. The solute formation energies of H and He are the lowest in the respective groups. Further, it is observed that the substantial endothermic formation energies of alkali (Li, Na, K, Rb), noble gas (He, Ne, Ar, Kr, Xe), alkaline earth (Mg, Ca, Sr) and halogen (F, Cl, Br, I) atoms are in accord with their immiscibility in bcc iron. Se, Ag and Cd too are immiscible in bcc iron. In agreement with this, the present calculation predicts large endothermic formation energies for these solutes. For elements, Al, Si, V, Cr, Co, Ge and As, the calculations predict exothermic formation energies. This is in line with their large solid state solubility in Fe. For other elements, H, Be, B, C, N, O, P, S, Sc, Ti, Mn, Ni, Cu, Zn, Ga, Y, Zr, Nb, Mo, Tc, Ru, Rh, Pd, In, Sn, Sb and Te, the calculations predict moderate endothermic formation energies. Among these, the solutes with appreciable solubility such as H, Be, N, P, Ti, Mn, Ni, Zn, Ga, Mo, Ru, Rh, Pd, Sn, Sb and Te have generally relatively lower formation energies than solutes with negligible solubility such as B, C, O, S, Sc, Cu, Y, Zr, Nb, Tc and In.

The interaction among atomic defects in a host matrix can have different components. The solute formation energy represents the chemical component which is usually the dominant component. The other component that is considered along with the chemical component is the strain component. The strength of the interaction due to the strain component is to a first approximation proportional to the size factor of the solute atoms in the solvent

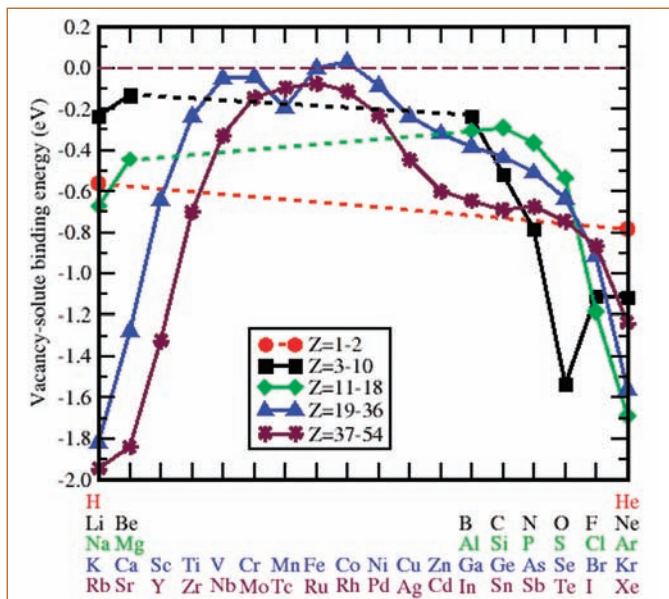
matrix. Therefore we computed the size factors of the solute atoms M in bcc Fe which is the effective size of the solute atoms in iron matrix relative to that of iron atom.

Figure 3 displays the size factors of the solute atoms M. Similar to formation energies, the size factors of the elements from fourth and fifth periods vary with their atomic numbers such that they reach maxima near the ends of the periods and broad minima in between, with a local hump near Ga and In. The size factors of solutes from second and third periods show a similar trend to the solutes near the ends of the fourth and fifth periods. The size factors of H and He are the lowest in their respective groups. The size factor of B deviates from this trend.

It is further evident that majority of solute atoms have positive size factors. That is, the effective size of these solute atoms in iron matrix is larger than that of iron atoms. This is in agreement with the increase in the lattice parameter of bcc iron with the addition of 3d solute elements. Furthermore, the elements that are identified to be immiscible according to their formation energies (He, Li, B, C, O, F, Ne, Na, Mg, S, Cl, Ar, K, Ca, Sc, Cu, Se, Br, Kr, Rb, Sr, Y, Zr, Pd, Ag, Cd, In, Sn, Sb, Te, I and Xe) also generally have large size factors. He, Li, C and S are exceptions. These elements are immiscible in iron despite their relatively small size factors. Al, Ti, V, Cr, Mn, Ni, Zn, Ga, Ge, As, Nb, Mo, Ru and Rh form another set of exceptions. These elements exhibit appreciable solubility though their size factors are relatively large.

Solute-Solute Binding Energy

In an alloy, solute atoms can move randomly in all directions. When they encounter one another, the interaction can be attractive or repulsive which would cause either precipitation or segregation. Therefore it is useful to obtain the binding energies of pairs of solute atoms in iron. Figure 4 depicts our calculated solute-solute binding energies. We see that the binding energies show a similar but inverse variation with respect to the atomic numbers like the solute formation energies shown in Figure 2. That is, strong binding energies occur for solute pairs at the ends of the periods and weak binding energies for pairs from the middle of the periods. Further, the relatively strong binding energies obtained for the alkali, alkaline earth, halogen, noble gas, Cu, Ag, Cd and S atoms suggest that the driving force for their segregation rather than remaining in solution is quite high which is in agreement with their immiscibility or limited solubility in bcc iron. Molecular dynamics simulation of He clustering and bubble



Vacancy-Solute Binding Energy

As mentioned earlier, the vacancy-solute binding energy is one of the important factors to control diffusion and solute solubility and hence clustering or nucleation of precipitates. They are also useful for modelling and predicting the mechanical behaviour of steels under irradiation. Therefore we have computed the binding energies of vacancy-solute pairs inserted in the bcc Fe matrix.

The binding energies of vacancy solute pairs in BCC iron is presented in Figure 5. As can be seen, the binding energies of vacancy-solute pairs show an approximately inverse variation, similar to solute-solute binding energy, with respect to the atomic numbers of the solutes compared to the solute formation energies shown in Figure 2. It is also noted that the binding energies of elements from fifth periods are generally stronger than those of elements from the fourth period. Further, the binding energies are attractive for all the solutes except Co.

Figure 5: The binding energies of vacancy-solute pairs in bcc Fe

formation in bcc Fe has shown that isolated He atoms are highly mobile and they aggregate into clusters. The binding energy calculated by us indeed suggests clustering of He atoms in Fe. The solute-solute binding energies computed in this work, further suggest that pairs of 3d and 4d atoms from Ti to Ni and Zr to Pd show a tendency to repel each other while Cu, Zn, Ag and Cd have a tendency to cluster. We also observe that the calculated binding energies are smaller for H, Be, Al, Mn, Co, Ni, Ga, Y, Tc, Ru and Pd pairs. Several of these solutes (Al, Co, Ni, Ga) are known to form extended solid solutions in bcc Fe.

Figure 6 is a graph of vacancy-solute binding energies of 3d and 4d transition metal atoms plotted with respect to their corresponding calculated diffusion coefficients. It is interesting to note that the binding energies show an inverse variation to the calculated tracer diffusion coefficients. The strong binding energies of solutes to vacancies in bcc iron further suggest the absence of slow diffusers among the common solute additions to bcc Fe.

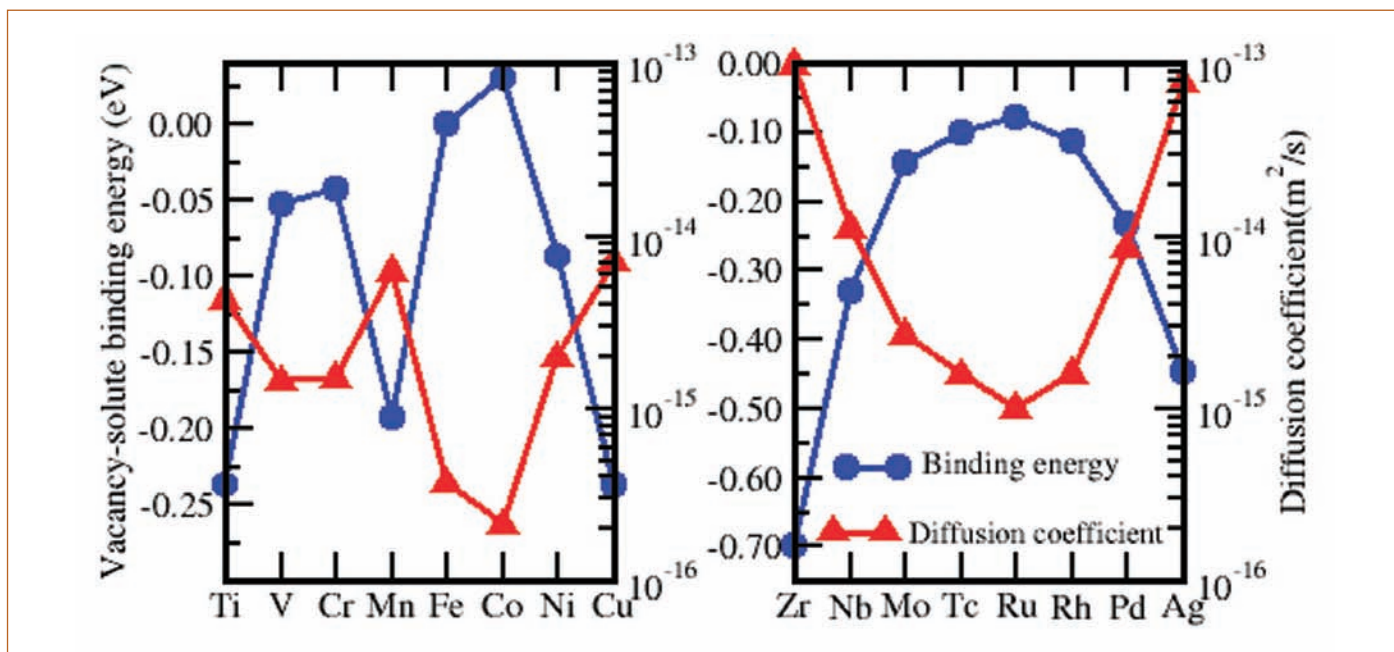


Figure 6: Graph of nearest neighbour vacancy-solute binding energies for 3d and 4d transition metal atoms plotted with respect to their diffusion coefficients

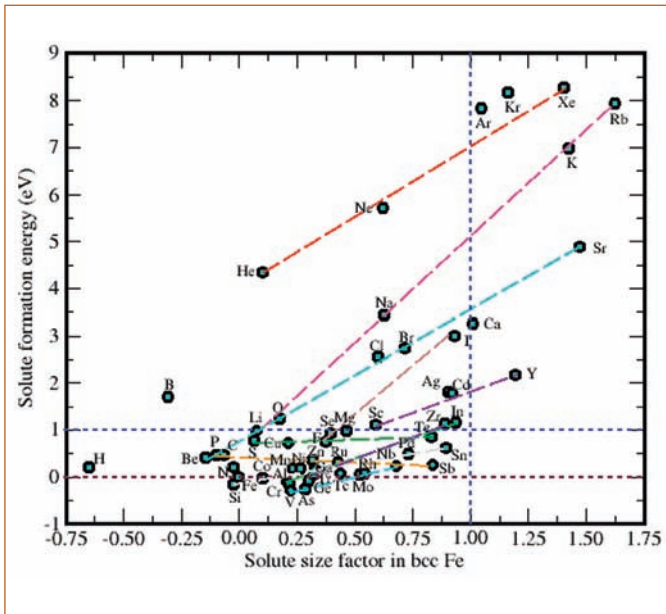


Figure 7: Solute formation energies versus their size factor in bcc Fe

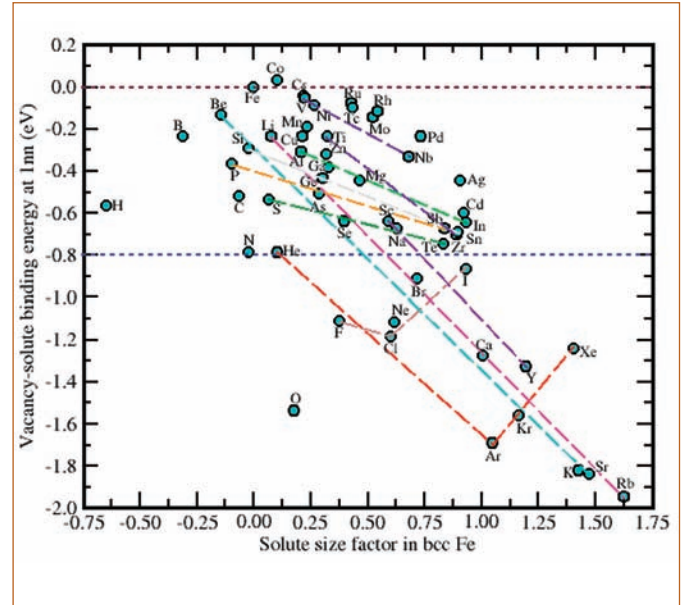


Figure 8: Graph of vacancy-solute binding energy versus solute size factor in bcc Fe

Discussion of Correlations

Comparison of formation energies of solute atoms with their size factors is displayed in Figure 7. It shows that the solute atoms which form alloys with iron generally have size factors below 1 and formation energies below 1 eV and those which do not normally alloy with iron (Li, Na, K, Rb, He, Ne, Ar, Kr, Xe, F, Cl, Br, I, Mg, Ca, Sr, Ag, Cd, In and Y) have solute formation energies above 1 eV. Further, comparison of isoelectronic solutes, indicated by long dashed lines in Figure 7, show that the size factor increases down the group with an associated increase in the solute formation energy. Solutes H, B, C, N and O are exceptions to this trend. Another physical trend that may be noticed is that the rate of increase of solute formation energy with the size factor is less along V/Nb, Cr/Mo, Mn/Tc, Co/Rh and Ni/Pd groups as compared to alkali, alkaline earth, halogen and noble gas atoms. The higher rate of increase of solute formation energies with size factors, for instance, for alkali elements or noble gas atoms, is likely due to the strain component of the interaction being more dominant than chemical component. This also indicates, for instance, that the solubility of He in iron would increase appreciably with pressure as compared to the solubility of Nb or Mo.

A graph of vacancy-solute binding energy versus solute size factor in bcc iron is shown in Figure 8. It is evident that the common alloying elements in steel have their vacancy-solute binding energies above -0.8 eV and size factors within -0.25 and 1. Figure 8 reveals other correlations as well. Isoelectronic sets of

solute atoms show a clear trend that the strength of the vacancy-solute binding energies increases with increasing size factor down the columns, as indicated by dashed lines. For halogen and noble gas elements, the vacancy-solute binding energies increase initially (F to Cl and He to Ar) with the size factors and then decrease with further increase in the size factors (Cl to I and Ar to Xe). This may be understood as follows: these atoms behave more like hard spheres in the iron matrix (unlike, for instance, alkali elements with a strong tendency to release electrons). The size factors of F and Cl as well as He, Ne and Ar are relatively smaller that they can relax their stresses by relaxing to the nearby vacancy site. But this is not effective for solutes with size factors beyond a certain limit (Br and I as well as Kr and Xe) which manifests in the reduction of their vacancy-solute binding. Interstitial solute atoms deviate from the group-wise correlations. Experimental solution enthalpies and size factors also show that the deviation of H, B, C, N and O is real. Thus the computed energetics of atomic defects in bcc Fe reveals several fundamental trends and will be useful for identifying solutes or combination of solutes with desired diffusion property that can be used to optimize the coarsening kinetics and creep-strength of steels.

*Reported by
Chinnappan Ravi, Materials Science Group*

Recovery of Actinides using Supercritical Fluid Extraction: A Green Separation Technique

Extraction and recovery of actinides from different process steps of nuclear fuel cycle operations is an important task in the nuclear industry. Selective extraction and separation of actinide species using different class of ligands has been the subject of continued research. The extraction and recovery of actinides is generally carried out using traditional separation techniques such as liquid-liquid extraction, ion-exchange, solid-phase extraction and chromatographic techniques. Though conventional methods are well established, however, use of these techniques results in the generation of organic waste (toxic, flammable and volatile) and radioactive secondary liquid waste, which requires further treatment. Therefore, there is strong impetus for the development of eco-friendly/green separation methods that can reduce waste generation and minimize the adverse effects on the environment.

In recent years, supercritical fluid extraction (SFE) based techniques have been advantageously exploited as an alternative to conventional methods to address various issues relating to separation technology. SFE finds wide variety of applications

in polymer processing, material processing, agriculture and food industry, hydrometallurgy, pharmaceutical industries and biotechnology. Some applications are already at industrial capacity, whereas others are under development. SFE is a technique that uses a supercritical fluid (generally supercritical carbon dioxide, SCCO_2) as a solvent for the extraction or separation of a compound of interest from a matrix. SFE has several advantages over conventional separation techniques such as i) reduction in the generation of toxic organic waste, ii) direct recovery of compounds from solid matrices, iii) fine-tuning the extraction behavior using experimental parameters etc.

SFE based methods are very attractive for the nuclear industry where radioactive waste management is an important task. The development of an SFE process for the recovery of actinide ions involves the following

- (a) Identification of actinide-specific ligands
- (b) Selection of ligand based on the nature of matrix in which the

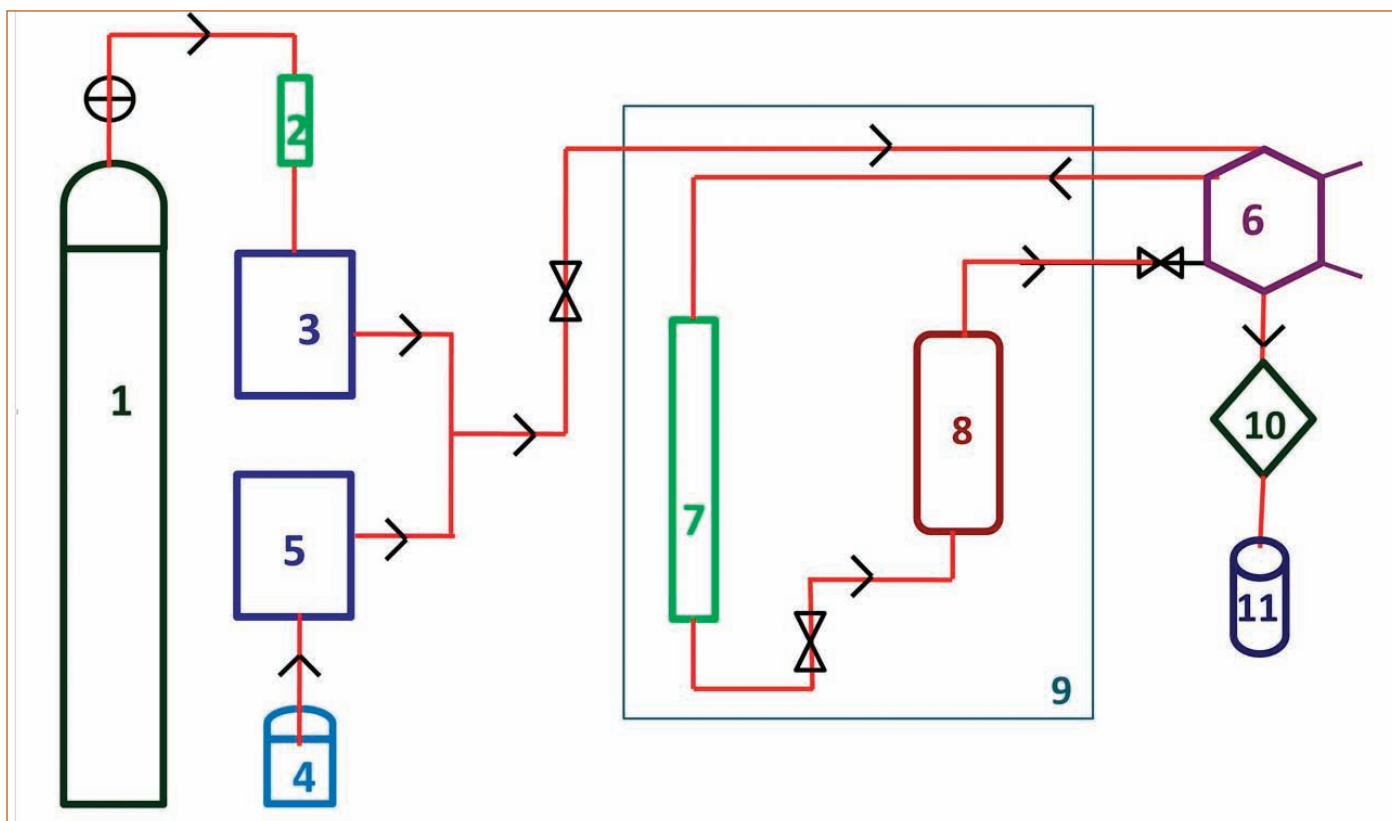


Figure 1: Schematic diagram of experimental set-up for the supercritical fluid extraction studies; (1) Carbon dioxide cylinder, (2) molecular sieve filter, (3) carbon dioxide pump, (4) co-solvent reservoir, (5) co-solvent pump, (6) six way valve, (7) heat exchanger, (8) High pressure extraction vessel (9) oven (10) back pressure regulator, (11) collection vessel

solute of our interest is present

- (c) Measurement of solubility of actinide specific-ligands in SCCO₂ medium
- (d) Use of SCCO₂ containing ligands for recovery of actinides
- (e) Optimization of experimental parameters such as temperature, pressure and modifier

Organophosphorus compounds (trialkyl phosphates, dialkylalkyl phosphonates, H-phosphonates, phosphinic acids etc), N,N-dialkyl amides, room temperature ionic liquids have been widely employed for the extraction of actinides from different environments. In our laboratory, we have developed SFE based methods for the recovery of actinides from a wide variety of matrices such as chloride salt matrices, polymers, cellulose, glass, stainless and teflon matrices with minimum generation of secondary liquid waste. Some important applications are discussed in this article.

1 Solubility of actinide-specific ligands in SCCO₂ medium

Solubility is the most important parameter affecting the efficiency of a SFE process. Solubility can have a direct impact on the rate, yield, design and economy of a particular extraction process. The determination of solubility of actinide-specific ligands in SCCO₂ medium is the first and fundamental step towards developing an efficient extraction process for the recovery of actinides from different methods. Optimization of supercritical experimental conditions like pressure, temperature and flow rate of SCCO₂ are carried out based on solubility data.

A dynamic flow apparatus (flow saturation technique) was set-up and a procedure was developed in our laboratory for solubility measurements of ligands in SCCO₂ medium. The reliability of the experimental set-up and procedures were tested by measuring the solubility of tributyl phosphate and trioctyl amine in SCCO₂ medium. For the first time in the literature, the solubility of various actinide-specific ligands (trialkyl phosphates, dialkylalkyl phosphonates, H-phosphonates, phosphinic acids, N,N-dialkylamides, ionic liquids etc.) was determined in SCCO₂ to establish their suitability in SFE process. The solubility of these compounds were determined at three isotherms 313, 323 and 333 K with pressures varying from 10 to 25 MPa. The results indicated that the above compounds can be employed in SCCO₂ medium for recovery of actinides. The effect of co-solvent (low molecular weight alcohols) along with SCCO₂ has been studied for efficient extraction. The solubility data generated is successfully employed for the development of SFE based methods for the recovery of actinides. The experimental determination of solubilities of

compounds in SCCO₂ medium at different temperatures and pressures is time consuming, necessitating suitable model correlations to predict the solubilities. The experimental solubility data is modeled using different semi-empirical and empirical models (Chrastil, Mendez-Teja, Bartle and models based on association theory coupled with activity co-efficient models etc.) for their prediction. Based on these investigations, it is possible to compute or predict the solubility of ligands at desired temperature and pressure using the correlation parameters. New models are also developed for the correlation of solubility of ligands in SCCO₂ medium in the presence of co-solvents using association theory coupled with activity co-efficient models. These models successfully correlated the solubility data with an average deviation of less than 10%.

2. SFE Methods for Recovery of Actinides

2.1 Recovery of Uranium and Plutonium from chloride salt matrices

Pyrochemical reprocessing involves use of molten salts (LiCl - KCl or NaCl-CsCl) for the separation of actinides from fission products. The electrolyte salt, after processing of few batches, will be loaded with alkali and alkaline earth metals and lanthanide fission products. Salt waste arising from this process also contains residual actinides. Disposal of such molten salts is of great concern and different techniques have been explored in the recent past for the decontamination of molten salts. These techniques generally result in the generation of secondary radioactive waste. SFE based method was developed for the recovery of U and Pu from pyrochemical salt matrix using SCCO₂ containing appropriate ligand (Experimental set-up is depicted in Figure 1).

The recovery of U and Pu from salt matrix (UCl₃-LiCl-KCl, PuCl₃-LiCl-KCl and UO₂Cl₂-NaCl-CsCl) posed lot of challenges and use of traditional ligands (trialkyl phosphates, diketones etc.) resulted in an incomplete extraction. This aspect has motivated us to study the effect of salt matrix on recovery of actinides and results have shown that uranium in chloride salt matrix could be present as anionic complexes e.g. UO₂Cl₄²⁻/ UCl₆³⁻. The Influence of ligand, salt matrix, temperature, pressure, co-solvent and HNO₃ concentration were examined for efficient recovery of actinides. The experimental investigations have shown that U and Pu exist as chloride complex, introduction of an ion-pair reagent, trioctyl methyl ammonium chloride (TOMAC), resulted in complete recovery of U and

Pu (Extraction mechanism is depicted in Figure 2). The complete recovery of uranium from $\text{UCl}_3\text{-LiCl-KCl}$ and Pu from $\text{PuCl}_3\text{-LiCl-KCl}$ $\text{UO}_2\text{Cl}_2\text{-NaCl-CsCl}$ matrix was demonstrated at 323 K and 20 MPa using SCCO_2 containing acid equilibrated TOMAC in the presence of n-propanol as co-solvent (Figure 3). Under similar experimental conditions, the extraction yield of plutonium from $\text{PuCl}_3\text{-LiCl-KCl}$ matrix was found to be low; however, the extraction yield of Pu increased with additional static equilibration period. The recovery of uranium from $\text{UCl}_3\text{-LiCl-KCl}$ cylindrical rod was also examined and the extraction yield was found to be a function of acid concentration and static equilibration period. A static equilibration period of 48 h and dynamic extraction of 2 h resulted in an extraction yield of $\sim 90\%$. Based on the results, recovery of uranium from $\text{UO}_2\text{Cl}_2\text{-NaCl-CsCl}$ matrix was carried out on a preparative scale SFE system, which resulted in an extraction yield of 85%. The studies have shown that SFE based technique can provide an excellent alternative to extract and recover actinides from chloride salt matrices.

2.2 Recovery of actinides from polymer matrices

Polymers are widely used and are indispensable in handling radioactive materials in fume-hoods, glove-boxes, etc. SFE based method was developed at our laboratory for the

recovery of actinides from different polymeric matrices such as neoprene, polyvinyl chloride (PVC) and surgical gloves using SCCO_2 containing n-octylphenyl-N,N-di-iso-butyl carbamoylmethylphosphine oxide (O_ϕCMPO).

The polymer matrices are initially subjected to neat SCCO_2 extraction to prevent co-extraction of organic compounds during the recovery of actinides. The extracts were analyzed by Infrared Spectroscopy (IR) and High Pressure Liquid Chromatography (HPLC). These results indicated the presence of some of the additives like plasticizers, dioctylphthalate, methacrylic acid and dioctyl sebatate in the initial extraction with SCCO_2 . The complete recovery of plutonium from simulated polymer matrices was achieved at 323 K and 20 MPa using SCCO_2 containing CMPO.

SFE on actual waste, i.e. plutonium present in polyvinyl chloride (PVC) matrix was carried out using 0.1 L extraction vessel in various batches and the extraction efficiency was found to be 97% (Figure 4). SFE method was also demonstrated for the recovery of americium from simulated neoprene waste matrix with an extraction efficiency of 99%. As the disposal of polymer waste is of major concern in nuclear waste management, the SFE technique developed in the present study offers a potential opportunity for the recovery of actinides with generation of minimum secondary waste.

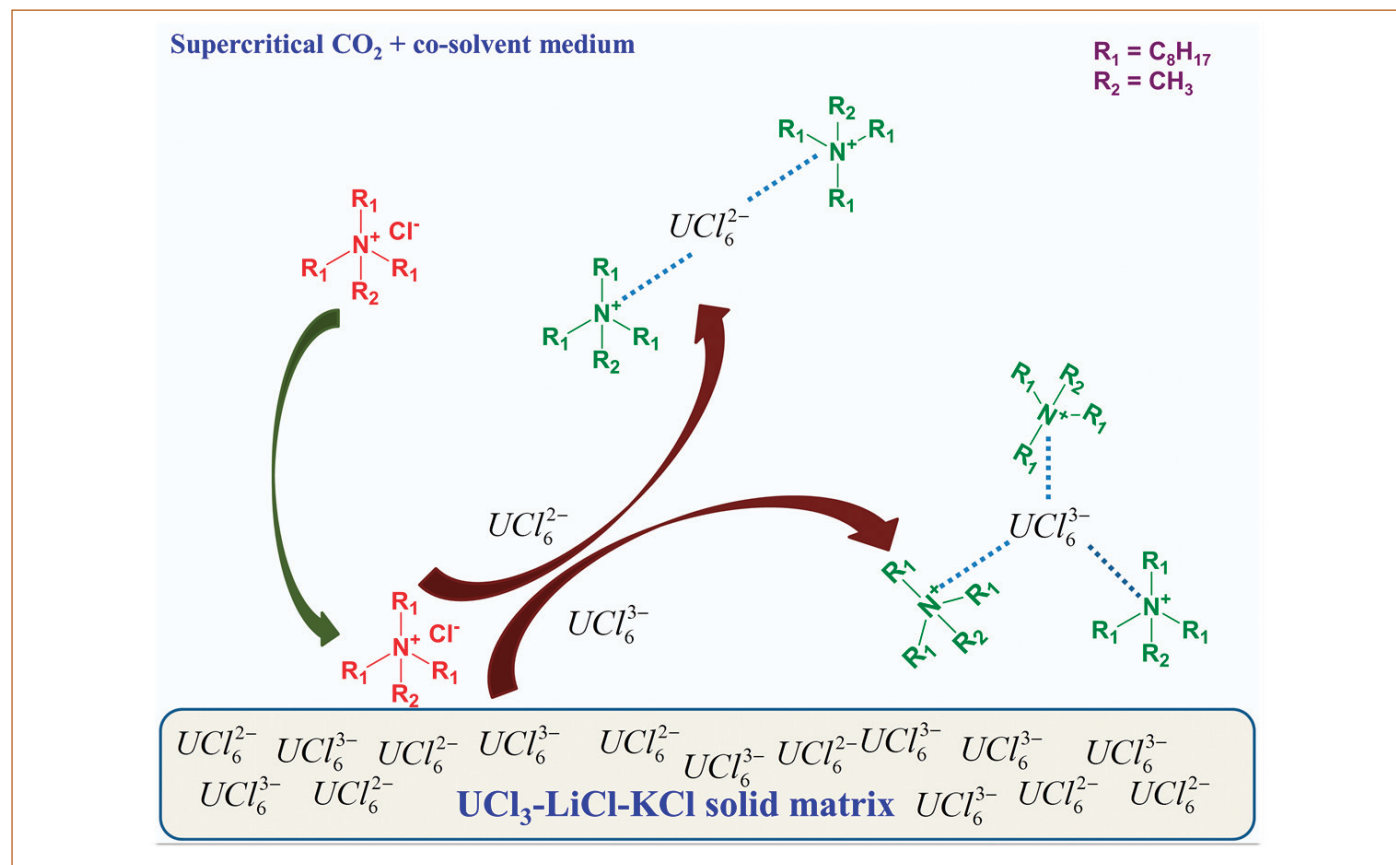


Figure 2: Extraction scheme for the recovery of uranium from $\text{UCl}_3\text{-LiCl-KCl}$ using SCCO_2 containing TOMAC in co-solvent

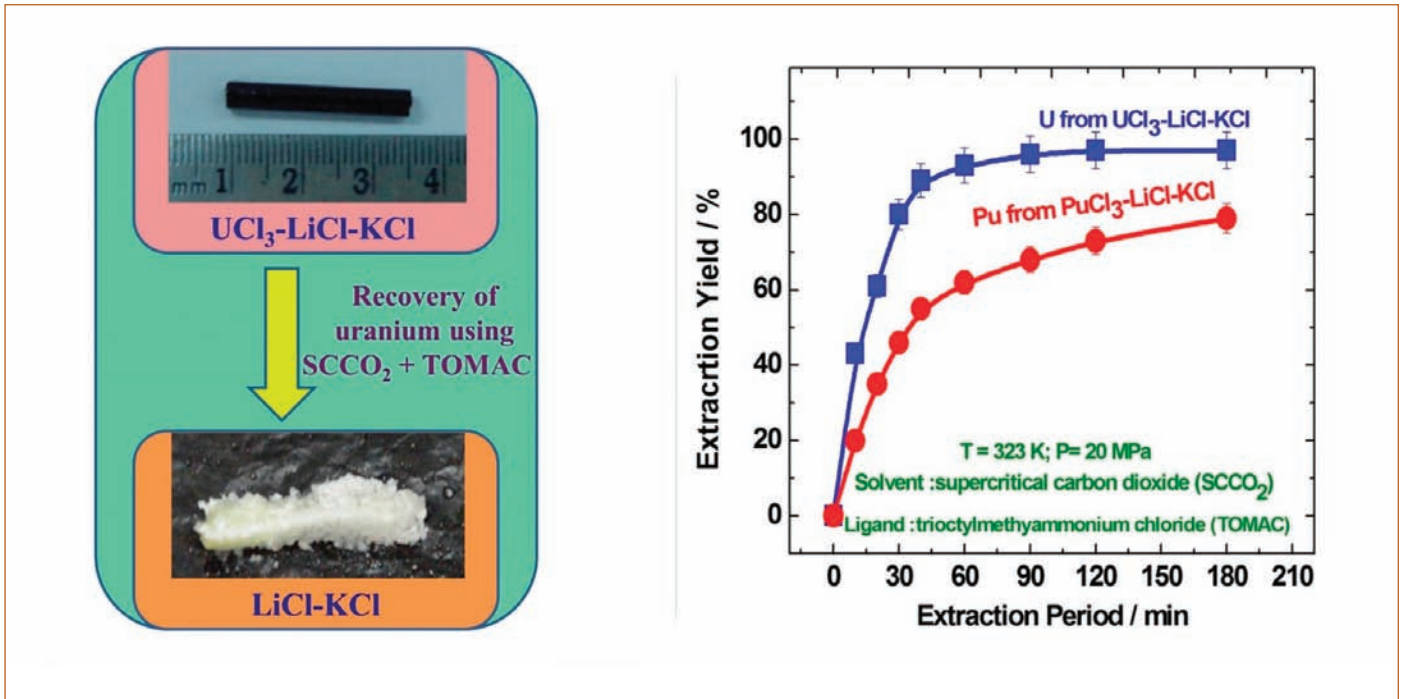


Figure 3: Recovery of U and Pu from chloride salt matrix using SCCO₂ containing TOMAC

2.3 Recovery of Uranium from fission products

Selective extraction of actinides from nuclear fuel dissolver solution is an important aspect of nuclear fuel reprocessing. Dissolver solution usually contains uranium, plutonium and fission product elements. SFE method has been developed for the selective extraction of uranium from fission products (La(III), Ce(III), Pr(III), Nd(III), Cs(I), Sr(II), Ba(II), Zr(IV) and Mo(VI)) using SCCO₂ containing phosphonates and phosphates. Phosphonate and phosphate based ligands are preferred over phosphine oxide

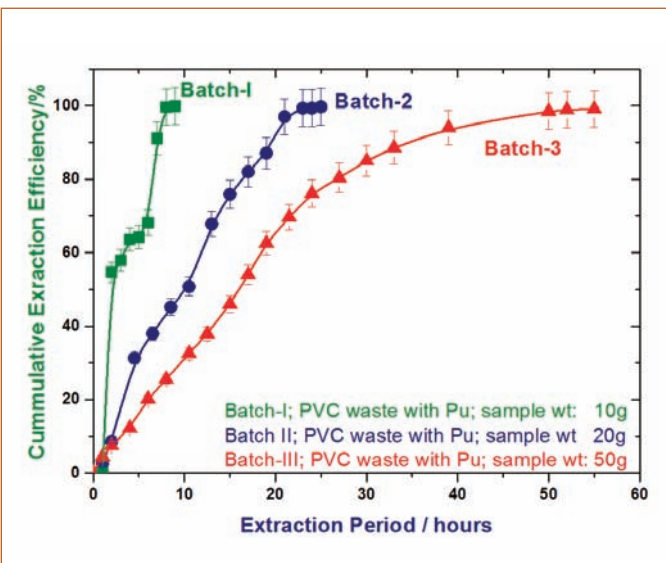


Figure 4: Recovery of plutonium from PVC matrix using SCCO₂ containing CMPO

based ligands due to the easy stripping of actinides as their nitrates from the extracted actinide-ligand complex.

SFE of uranium and representative fissions products was investigated in 4 N HNO₃ medium using tri-*iso*-amyl phosphate (TiAP). Studies established that a minimum of 45 minutes of static extraction followed by 1 hour of dynamic extraction were required for the complete extraction of uranium from nitric acid medium. The results of extraction of uranium from selected fission products from nitric acid media using TiAP at 323 K and 20 MPa are summarized in Table 1. The extraction efficiency of uranium was found to be about 95%. Metal ions such as lanthanides, Ba(II) and Cs(I) were not extracted under the experimental conditions, where near complete extraction of uranium was obtained. The extraction efficiencies for Sr(II), Zr(IV) and Mo(VI) were found to be 5, 8 and 6% respectively. Similar extraction behavior was reported for lanthanides, Cs(I), Sr(II), Ba(II), Zr(IV) and Mo(VI) by employing phosphonates as a complexing agent. The present study indicated selective extraction of uranium in the presence of fission products from the nitric acid medium and can be achieved using phosphates and phosphonates. The selectivity of uranium from representative fission products is mainly due to their relative differences in distribution coefficient values. The solvent extraction studies reported in the literature indicated that TiAP has higher distribution coefficient for U(VI) over fission products. At 4 N HNO₃ medium, for tracer solution, distribution coefficient for U(VI) for uranium is 35.2; under similar

experimental conditions, the distribution ratios for La(III), Ce(III), Nd(III) and Zr(IV) are 0.017, 0.021, 0.033 and 0.44 respectively. These results have established phosphonates and phosphates as the potential candidate materials for the selective recovery of U(VI) from fission products in SCCO₂ medium.

Table 1: SFE of uranium from simulated fission products using TiAP

	Metal ion	Extraction efficiency # (%)
	UO ₂ ²⁺	95
Representative Fission Products	La ³⁺	<3
	Ce ⁴⁺	<3
	Pr ³⁺	<3
	Nd ³⁺	<3
	Cs ⁺	<2
	Ba ²⁺	<2
	Sr ²⁺	5
	Zr ⁴⁺	8
	Mo ⁶⁺	6

Experimental conditions: temperature: 323 K, pressure: 20 MPa; SCCO₂ flow rate: 2.5 mL/min; Sample: uranyl nitrate + fission product elements in 4 N HNO₃ medium; volume of extraction vessel: 10 mL; static extraction: 1 hour and dynamic extraction: 1 hour #Extraction efficiency is an average of three independent experiments with a relative standard deviation of less than 5%.

2.4 Recovery of U and Th from acidic waste

The extraction and recovery of U(VI) and Th(IV) from acid waste is of importance as these ions have many important applications in nuclear fuel cycle as well as it reduces radiological waste burden. Different SFE based methods were developed and demonstrated for the recovery of U and Th from nitric acid medium using SCCO₂ containing series of organophosphorous compounds (trialkyl phosphates, dialkylalkyl phosphonates and trialkyl phosphine oxides).

Selective recovery of uranium from thorium matrix (e.g. irradiated ThO₂ fuel) is an important process and it has been examined using SCCO₂ containing (a) trialkyl phosphates, (b) dialkyl alkyl phosphonates and (c) trialkyl phosphine oxides. These ligands

are taken-up as these are traditionally used in solvent extraction experiments. The results on the relative extraction of U(VI) and Th(IV) from 4N HNO₃ medium are represented in Table 2. Among the ligands employed in the present study, TsBP offers better separation factor and the trend is similar to the results observed with solvent extraction studies. The better separation factor observed with TsBP is due to the branching of substituents in TsBP that cause tri-solvated thorium to be less stable and hence aids in the preferential extraction of U(VI) over Th(IV). These studies have also demonstrated the viability of using different organophosphorous compounds in supercritical medium for the recovery of actinides from liquid nuclear waste.

Table 2: Extraction efficiency of uranyl and thorium nitrates from 4 N nitric acid medium using organophosphorous compounds

Sl.No	Ligand	Extraction efficiency * (%)	
		U(VI)	Th(IV)
1	Tributyl phosphate (TBP)	74	19
2	Tri-sec-butyl phosphate (TsBP)	84	7
3	Tri-iso-amyl phosphate (TiAP)	78	38
4	Dibutyl butyl phosphonate (DBBP)	88	45
5	Diamylamyl phosphonate (DAAP)	87	28
6	Trioctylphosphine oxide (TOPO)	91	87

Experimental conditions: temperature: 323 K, pressure: 25 MPa; SCCO₂ flow rate: 2.5 mL/min; Sample: uranyl nitrate + thorium nitrate in 4 N HNO₃ medium; sample loaded: 0.01 mmol each; ligand loaded: 0.94 mmol; volume of extraction vessel: 10 mL; static extraction: 1 hour and dynamic extraction: 1 hour; *Extraction efficiencies are an average of three independent experiments with a relative standard deviation of 5 %

The above studies have established promising applications of supercritical fluid extraction based methods for the recovery of actinides from diverse matrices with minimum generation of liquid secondary waste.

Reported by

K. C. Pitchaiah and colleagues, MC&MFCG

Young Officer's FORUM

Plant Dynamics Modeling of Inadvertent Closure of Sodium Side Isolation Valve of a Single SG in a SFR



Shri. G. Vikram completed BE in mechanical engineering from College of Engineering, Guindy. Then he joined OCES training from 9th batch of BARC training school at IGCAR campus. After successful completion of training, he joined the Thermal Hydraulics Section of the then Reactor Design Group in 2015. Since then, he has been working in the field of plant dynamics and safety analysis of Sodium cooled Fast Reactors (SFRs) with the help of system thermal hydraulics codes. He completed M. Tech. in the field of sodium boiling simulation from Homi Bhabha National Institute.

Studies on plant dynamics involves simulation of the nuclear power plant dynamic processes and their responses under abnormal events. These studies contribute significantly in conceptual design of systems, detailed design of components, safety demonstration of plant towards licensing, development of computer models that drives the simulator for operator training,

devise safe and simplified operating procedures etc. Traditionally, plant dynamics studies are carried out using one-dimensional codes known as plant dynamics codes. They have computational models for representing different physical phenomenon in the entire plant, viz., (i) core kinetics model to simulate neutronic phenomenon in the core (ii) core thermal model to simulate heat

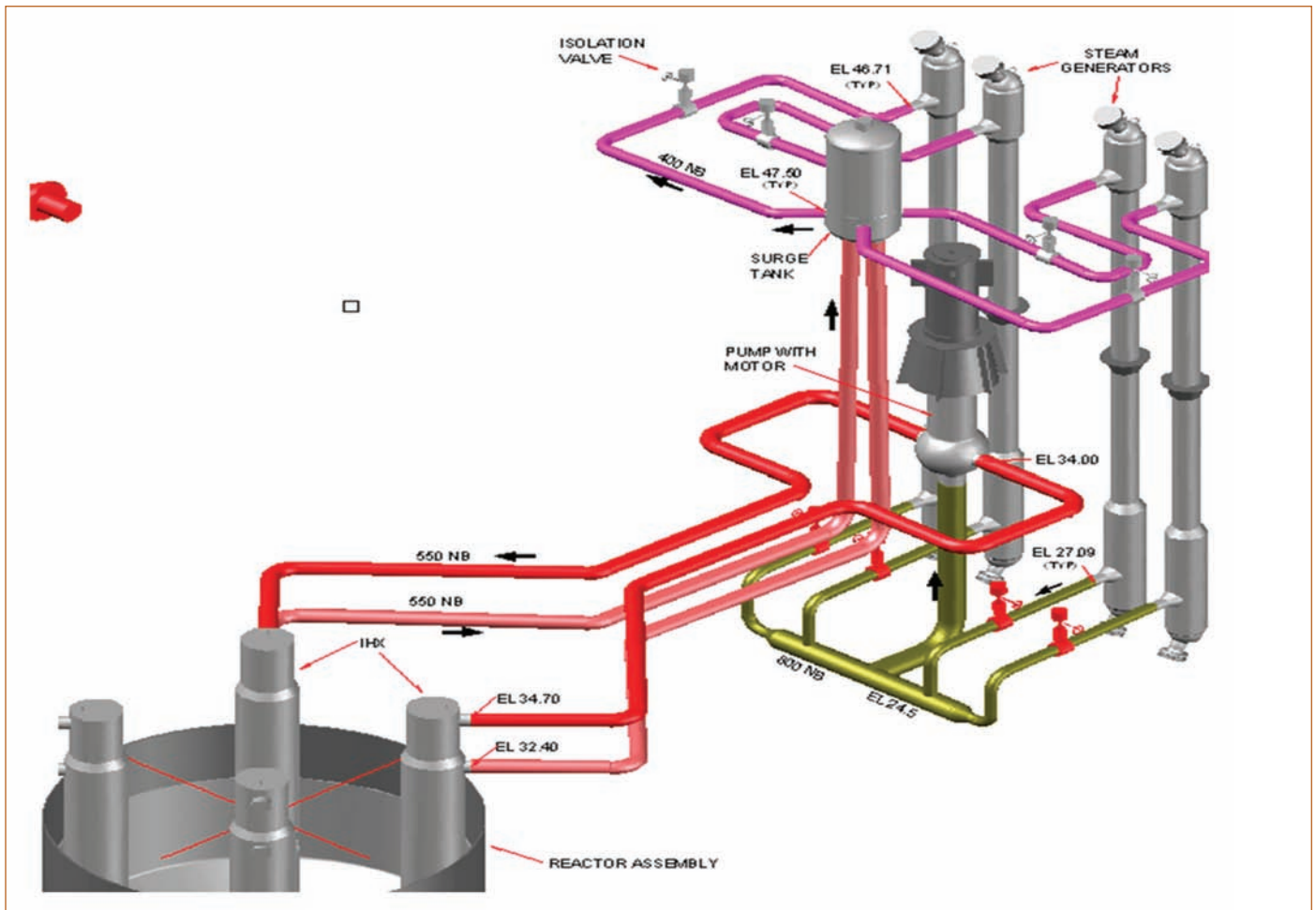


Figure 1: Secondary Sodium Circuit Layout

transfer phenomenon in the core (iii) heat exchanger thermal model to simulate heat transfer phenomenon in heat exchangers (Intermediate Heat Exchangers, Steam generators etc.) (iv) piping thermal model to simulate heat transfer phenomenon in sodium pipelines (v) hydraulics model to simulate sodium flow evolution in coolant circuits (vi) plenum thermal model to simulate coolant mixing phenomenon in sodium pools (vii) torque balance model along with performance and cavitation characteristics for representing sodium pumps etc. DYANA-P is the plant dynamics code having all the above-mentioned models developed in-house for carrying out the plant dynamics studies for pool type sodium cooled fast reactor (SFR).

In a typical medium sized SFR, there are three heat transport circuits between the reactor core and turbine. These are primary, secondary and tertiary/steam-water circuits. Liquid sodium is the coolant in primary and secondary circuits while it is water in the tertiary circuit. In general, there are multiple Steam Generator (SG) modules in each secondary circuit of the reactor that transfer heat from the secondary to the tertiary circuit. SG are shell and tube heat exchangers with sodium on the shell side and water on the tube side. There are isolation valves (Figure 1) installed in the inlet and outlet pipes connecting the shell side of each SG to stop the sodium flow through the SG in case of any water leak in it to mitigate the consequences of sodium-water reaction. With these valves, it is also possible to continue the reactor operation at a reduced power by isolating the affected SG from the circuit. In case of spurious closure of an isolation valve of an SG, the shell side sodium flow would be stopped in that SG and there would be a reduction in the heat removal capability of the plant. The resulting effects could be propagated to primary sodium circuit through sodium pipelines and IHX. The plant adopts a feedwater flow control system based on the heat removal performance of

each secondary sodium circuit as a whole. Individual SG module-based feedwater flow control is not adopted for simplicity of design. Therefore, the temperature of steam/water coming out of different SG units would be significantly different and there could be a concern on the steam header integrity where all these flowing streams mix together. Hence, it becomes important to evaluate the thermal hydraulic consequences of this event on the reactor core and other parts of the plant.

Code Modifications

The secondary circuit hydraulics model of DYANA-P employs network based integral momentum approach to model the evolution of sodium flow rate in the circuit. In the previous version of DYANA-P, each secondary sodium circuit was modeled considering two segments. The governing equations for secondary sodium circuit hydraulics were obtained by making momentum balances between surge tank outlet to pump tank inlet through all the four SG modules together and pump tank inlet to surge tank inlet through secondary sodium pump (SSP) and IHX. Additionally, mass balance for surge tank and torque balance for secondary sodium pumps shaft are considered. This kind of modeling is sufficient for simulating various events in which all the SGs behave identically. However, for the one SG isolation event, the branches with affected and unaffected SG modules need to be modeled separately. Hence, code modifications were carried out by formulating momentum balance equations for each SG line separately and mass balance equations at each junction (surge tank and SG sodium outlet header) and solving them simultaneously using Hamming's Predictor Corrector Method (HPCG solver). Also, the SG thermal calculations are carried out separately for each SG module in the loop. Earlier SG thermal calculations were carried out for only one representative SG in a

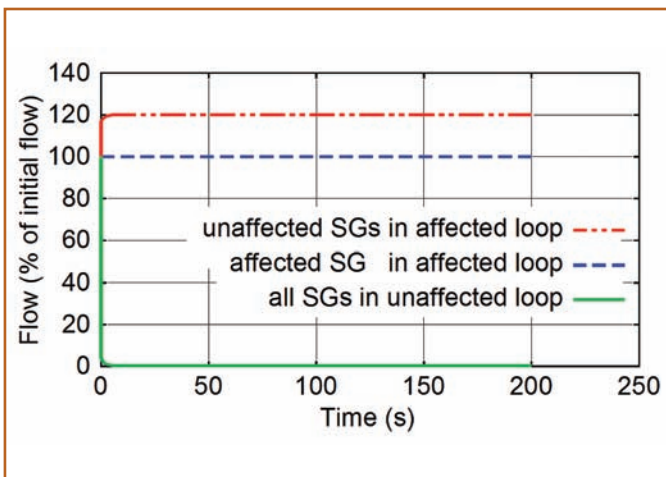


Figure 2: Evolution of Sodium Flow Rates in SGs

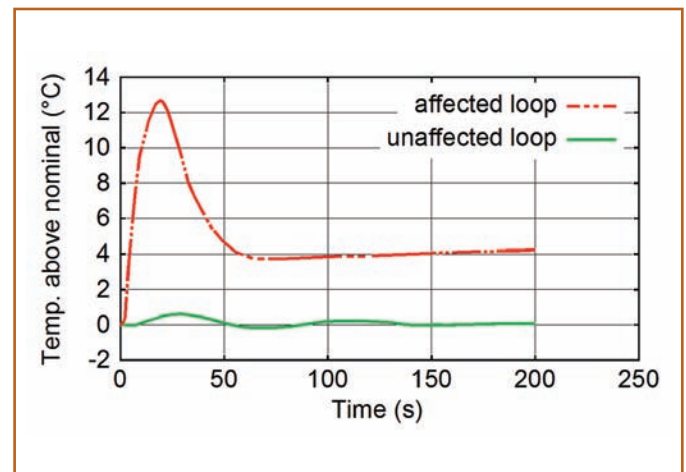


Figure 3: Evolution of Sodium Temperature at SG Outlet

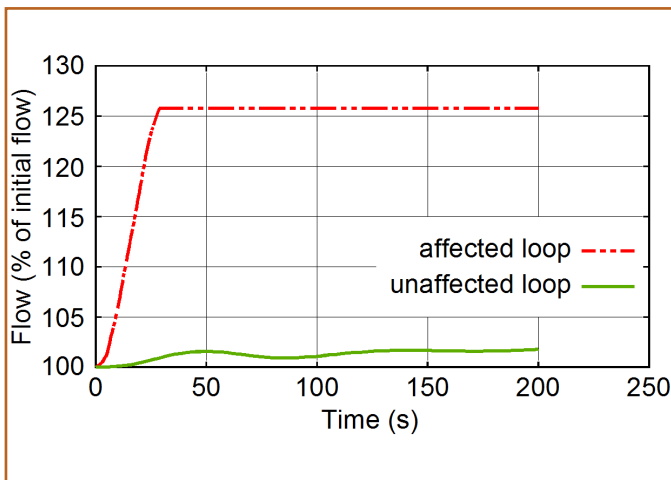


Figure 4: Evolution of Feedwater Flow Rate in SGs

loop. The temperature at SG sodium outlet header is calculated by perfect mixing assumption of flow streams from all the SGs in a loop.

With the new code, the event of inadvertent closure of sodium side isolation valve of a single SG in a typical medium sized SFR is simulated. The valve closure is simulated by increasing the flow resistance of a pipeline in the flow path of one SG alone to a very high value. The flow resistance is increased linearly over a duration of 10 s (a typical duration for the closure of the SG shell side isolation valves in SFRs from pressure surge considerations in the pipelines). The SG whose valve closure is simulated is designated as 'affected SG' while the other SGs are designated as 'unaffected SGs'. Similarly, the secondary sodium loop with the affected SG is designated as 'affected loop' and the other loop is designated as 'unaffected loop'.

Results and Discussion

The sodium flow evolution in SGs in terms of percentage of initial flow is shown in Figure 2. The sodium flow decreases in affected SG while it increases in unaffected SGs. However, the total flow in the circuit decreases ($\sim 90\%$ of nominal flow) due to effective increase in overall flow resistance in the path from surge tank to pump inlet.

The feedwater flow is uniformly varied in all the SGs of a loop by a feedwater flow controller (modeled as a PI controller in DYANA-P code) which tries to maintain the sodium temperature at the common outlet header of all SG modules in a loop at its nominal value. Due to reduction of heat sink, the sodium outlet temperature in the affected loop increases (Figure 3). Thus, feedwater flow rate also increases (Figure 4). After some time, the flow becomes constant at $\sim 125\%$ of the nominal flow which

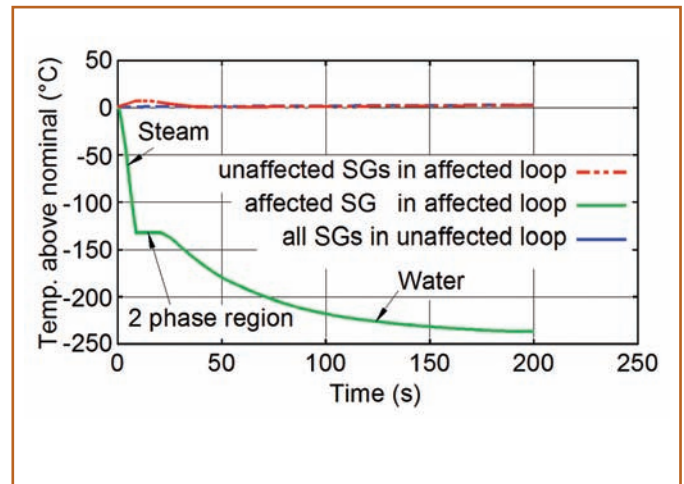


Figure 5: Evolution of water/steam temperatures at SG outlet

is the maximum possible flow increase considered in the analysis.

The evolution of sodium temperature at the SG sodium outlet header above its nominal value is shown in Figure 4. In the affected loop, this temperature is governed by the sodium outlet temperatures of unaffected SGs. It increases initially due to the decrease in total heat transfer in the affected loop. Subsequently, it decreases due to the feedwater flow increase caused by the action of feedwater controller. Finally, it stabilizes at about $4\text{ }^{\circ}\text{C}$ above the initial value. In the unaffected loop, the temperature stabilizes close to the nominal value. The initial oscillation is due to oscillation in the feedwater water flow caused by the action of feedwater controller.

The feedwater outlet temperature from the SGs above the nominal value is shown in Figure 5. In the affected SG, the feedwater outlet temperature decreases continuously as the heat transfer to feedwater decreases due to the decreased flow rate of sodium. It asymptotically reaches the feedwater inlet temperature by itself. It is also noted that the steam outlet temperatures from the unaffected SGs in the affected loop also reach the nominal temperature values due to the action of feedwater controller. In the unaffected loop, there is no significant change observed in this temperature.

The difference in temperature between the flow streams at the SG outlet from the affected and the unaffected SG modules would asymptotically reach a value equal to nominal water/steam temperature rise across the SG ($\sim 250\text{ }^{\circ}\text{C}$) at about 200 s from the event initiation. This temperature difference and time duration are critical for this postulated event and the damage to the steam header of the affected loop depends on these parameters.

The difference in temperature between the primary sodium outlets

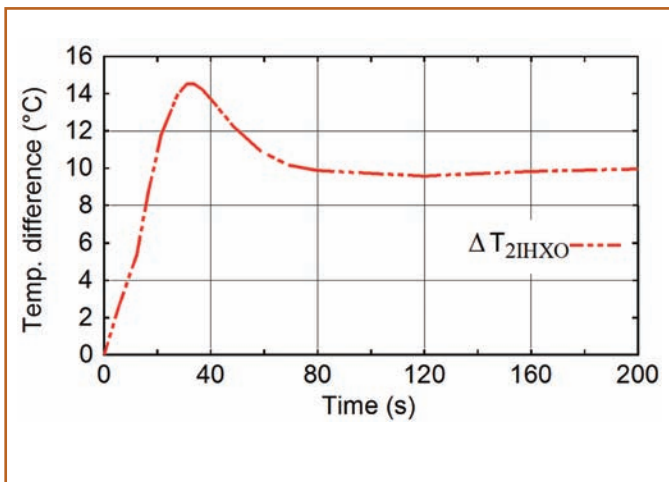


Figure 6: Evolution of ΔT_{2IHXO}

from the IHXs of the affected and unaffected loops is represented as ΔT_{2IHXO} . It is important to examine this temperature difference as it would produce unsymmetrical temperature distribution in the cold pool of the reactor. Evolution of this parameter is shown in Figure 6, which shows that there is no significant issue from this parameter as the maximum temperature difference is only about 15 °C and later it stabilizes at 10 °C.

The increase in the sodium and clad hot spot temperatures in the core due to increase in cold pool temperature is marginal (~3 °C). These temperatures are well below their design safety limits and there is no concern for core safety during this event.

Indications of Event Occurrence

Although there is no safety concern from the occurrence of the event in short term, the occurrence of the event has to be alerted to the operator so that corrective action can be taken to minimize the damage to steam header and other structures.

There are a set of plant parameters called SCRAM parameters that are monitored continuously and are engineered to trigger automatic trip of reactor once their value crosses the pre-set threshold values. Out of various SCRAM parameters that are present in a typical SFR, θ_{RI} (High Reactor Inlet temperature) is the parameter expected to be the most effective one during this event. Evolution of θ_{RI} parameter measured at the inlet of two primary sodium pumps in the circuit (θ_{RI1} and θ_{RI2}) during this event is shown in Figure 7. Cold pool temperature increases as the IHX primary sodium outlet temperature in the affected loop increases due to reduction in secondary sodium flow rate and increase in secondary sodium temperature in that loop. However, the rate of this increase comes down as the power is reduced due to feedback effect and ultimately hot pool temperature would have also reduced. It is observed that, θ_{RI1} representing the

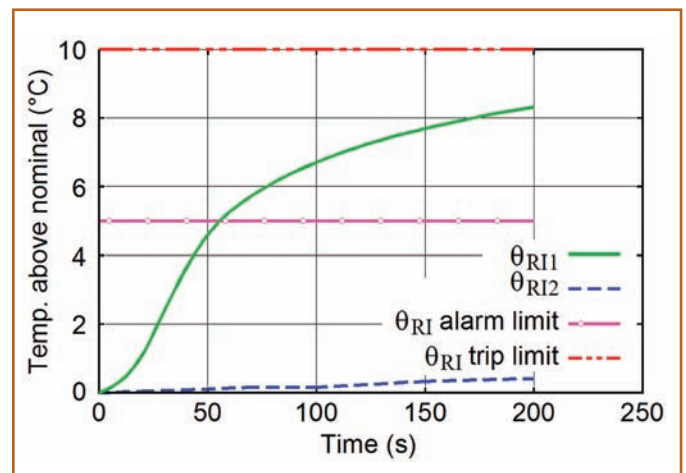


Figure 7: Evolution of Reactor Inlet Temperature Signal

temperature of primary sodium at the inlet of first primary sodium pump increases faster while θ_{RI2} is almost constant. At ~55s, there would be an alarm from θ_{RI1} signal (considering a typical alarm threshold value of 5 °C above the nominal temperature). θ_{RI1} increases by about 8 °C at the end of 200 s.

Apart from this, alarm will also be available from the limit switch of isolation valve almost immediately following the event initiation to alert the operator regarding the occurrence of the event to take corrective action.

Hence, for this postulated event, there would not be any automatic SCRAM parameter evolved (considering a typical SCRAM threshold value of 10 °C above the nominal temperature for this parameter). However, two independent alarms are available based on which the operator has to act manually. Moreover, there is no concern on core safety during this event.

Main concern of spurious closure of isolation valve in the sodium side of single SG module is the thermo mechanical loading arising due to feed water/steam streams of widely varying temperature exiting from the affected and the unaffected SG modules mixing in the outlet header. However, this condition prevails only for a short duration till manual action is taken by the operator. Two different alarms, viz., (i) temperature increase at the reactor inlet (at the pump inlet near the IHX of affected loop) and (ii) limit switches of isolation valves are available during this event to alert the operator regarding the occurrence of the event. Based on this, the operator shall manually trip the reactor. And there are no serious consequences to the core safety from this event as all the core temperatures reached are well below the design safety limits.

Reported by

G. Vikram, Reactor Design & Technology Group

Young Researcher's Forum



Shri Surojit Ranoo is working as a senior research scholar in Smart Materials Section, CSTD, MCG, MMG, IGCAR. He acquired M.Sc. in physics from Burdwan University, West Bengal and joined IGCAR in 2015, registered for PhD with HBNI under the guidance of Dr. John Philip. His research interest includes magnetic fluid hyperthermia and modelling dynamic magnetic responses at nanoscale. He has authored/coauthored 10 journal publications and is the recipient of the Best Poster Award, International Conference on Magnetic Fluids, Paris, 2019 and DST-AWSAR award-2019 for his contributions to magnetic fluid hyperthermia.

A Novel Approach to Enhance Magnetic Field Induced Heating Efficiency in Magnetic Fluids Through *in-situ* Orientation

Magnetic fluid hyperthermia (MFH) using superparamagnetic nanoparticles (SPM MNPs) have attracted considerable research interest in recent times, due to its applications in cancer therapy, field induced distal guidance, low clinical side effects and superior *in-vivo* efficiency. In MFH, magnetic nanofluids (dispersions of SPM MNPs) are injected into the cancerous tissues and thereafter exposed to a radio frequency alternating magnetic field (RFAMF), which causes the fluid/tissue temperature to increase. When subjected to a RFAMF, SPM MNPs undergo Neel-Brown relaxations, where magneto-thermal conversion of energy occurs during randomization of magnetic moments on field withdrawal and whole scale rotation of the MNPs, respectively. It has been reported that a temperature increase beyond 42°C aids in cancer therapy and by providing targeted thermal dose, MFH achieves superior and selective cancer therapy sans any significant side effects. Though *in vivo* efficiency of MFH has been reported in a few studies, there exists a wide gap in preparing ideal SPM MNPs with high heating efficiency. The size, shape, anisotropy energy density and magnetization of the MNPs along with medium viscosity and colloidal stability of the prepared magnetic nanofluids (ferrofluids) significantly influence the heating efficiency.

However, during practical applications of MFH in cancer therapy, the MNP dispersions are injected into the cancerous tissues and an increased medium viscosity in the tissue-like environment leads to the immobilization of the MNPs resulting in a loss of heating efficiency due to the abrogation of Brownian relaxation, which is undesirable for medical applications. Under such a scenario,

enhancement of the heating efficiency by varying explicit parameters like amplitude (H) and frequency (f) of RFAMF is not practical due to the physiological limit on $H.f < 4.85 \times 10^9$ A/m s. This calls for further studies towards development of better methodologies to increase the heating efficacy of SPM MNPs. As an alternative, an external DC magnetic field induced *in-situ* texturing method is proposed here, which increases the heating efficiency due to an enhancement in effective anisotropy energy density.

Experiments were performed on an aqueous ferrofluid containing phosphate coated Fe_3O_4 MNPs, synthesized in-house by a standard chemical process. The MNPs were characterized using powder X-ray diffraction and transmission electron microscopy. The average crystallite and particle sizes were found to be $\sim 7.7 \pm 0.8$ nm and $\sim 7.9 \pm 1.6$ nm, respectively. The hydrodynamic size and zeta potential were measured using dynamic light scattering (DLS) and were found to be ~ 33 nm and -31 mV, respectively. The presence of small aggregates was also confirmed using atomic force microscopy (AFM) imaging of the *in-situ* dried ferrofluid and the average topographic height was obtained as ~ 31 nm. Room temperature magnetization studies indicated the superparamagnetic nature of the MNPs, i.e. zero coercivity and high saturation magnetization (~ 52 emu/g). The temperature dependent magnetization studies under zero field cooled (ZFC) and field cooled (FC) protocols, indicated a blocking temperature around ~ 86 K. Assuming uniaxial anisotropy, the obtained value of the blocking temperature was utilized to estimate the anisotropic energy density of the MNPs, which was estimated as ~ 124 kJ/m³.

The RFAMF induced heating studies were performed using a high frequency induction heating system equipped with a water-cooled copper induction coil. RFAMF induced heating studies were carried out at a fixed frequency of 126 kHz over a range of magnetic field amplitudes varying from 22.2 to 33.1 kA/m. The field induced increase in ferrofluid temperature was measured using a radio frequency immune fiber optic temperature sensor. An experimental set-up was developed for *in-situ* orientation of the MNPs in dispersions, using two permanent magnets. Using this unique experimental set-up, the ferrofluids were simultaneously subjected to the RFAMF and a static magnetic field, thereby simultaneously achieving RFAMF induced heating and *in-situ* orientational ordering along the direction of the external DC magnetic field.

When dispersions of SPM MNPs are exposed to an oscillating magnetic field, the magnetic power dissipation (P), under linear response regime, is expressed by the equation:

$$P = \mu_0 \pi f H^2 \chi_0 \frac{2\pi f \tau}{1 + (2\pi f \tau)^2} \quad (1)$$

where μ_0 , H , f , and χ_0 indicate magnetic permeability of free space, RFAMF amplitude, RFAMF frequency and ensemble averaged equilibrium susceptibility, respectively. The effective relaxation time (τ) is expressed as $\tau^{-1} = \tau_N^{-1} + \tau_B^{-1}$, where τ_N and τ_B indicate the characteristic Neel and Brownian relaxation times, respectively. Experimentally heat dissipation is quantified in terms of a dosimetric quantity known as specific absorption rate (SAR), which is defined as the rate of power dissipation per unit mass of MNP. SAR values are estimated using the equation: $SAR = \frac{c \rho}{m} \left. \frac{dT}{dt} \right|_{t=0}$, where c , ρ and m indicate the specific heat, density and magnetic mass per unit volume of the ferrofluid, respectively. The quantity, $\left. \frac{dT}{dt} \right|_{t=0}$ is the initial rate of temperature rise, which is experimentally determined from linear regression analyses of the initial data points of the temperature rise curves. Figures 1a-b show the typical temperature rise ($\Delta T = T - T_R$, T_R being the reference temperature ~ 28 °C) curves for the oriented and random ferrofluids with MNP concentrations of 6 wt. %. It can be observed from Figures 1a-b that the rate of temperature rise was greater for the higher RFAMF amplitude, which was in

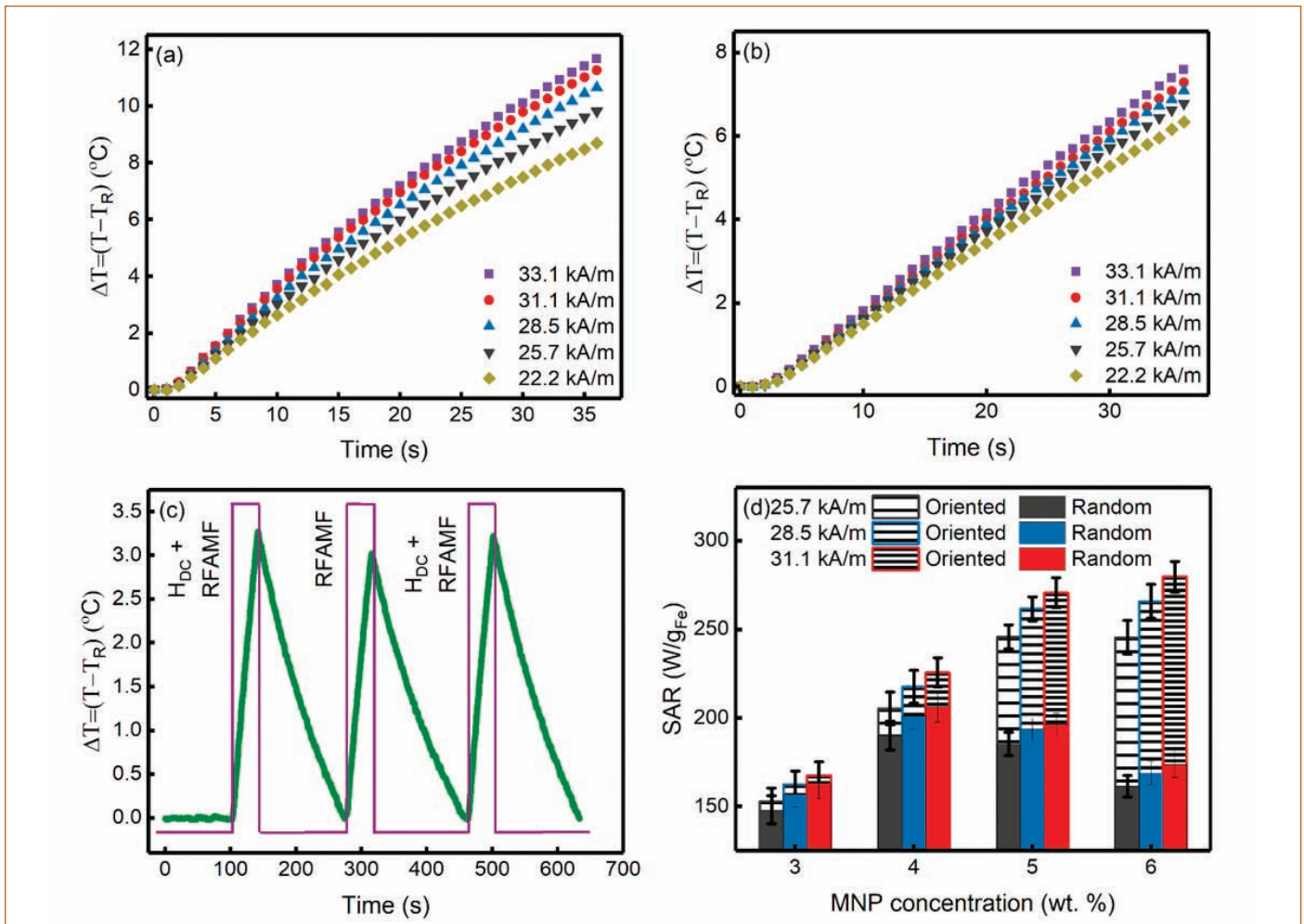


Figure 1: Typical temperature rise curves for the (a) oriented and (b) random ferrofluids (MNP concentration ~ 6 wt. %) at various RFAMF amplitudes. (c) Consecutive thermal cycling of the ferrofluid with MNP concentration of 3 wt. % with or without external DC magnetic field (H_{DC}). (d) A bar chart showing the SAR values at RFAMF amplitudes of 31.1, 28.5 and 25.7 kA/m for the oriented and random ferrofluids

agreement with linear response theory ($P \sim H^2$). It can be further seen from Figures 1a-b that ΔT increased monotonically with time and the rate of temperature rise and the maximum temperature rise, at the end of heating period, were higher for the oriented ferrofluids. This indicated a higher RFAMF induced heating efficiency for the oriented samples, which was due to the formation of linear chain-like structures along the direction of the external DC magnetic field, as subsequently discussed. Figure 1c shows the temperature rise during three consecutive RFAMF pulses, with or without the presence of the external DC magnetic field (H_{DC}). It can be seen from Figure 1c that withdrawal of H_{DC} , resulted in retrieval of the original temperature rise curve, where the MNPs were randomly redistributed in the aqueous medium. This further indicated the reversible nature of H_{DC} induced disorder-to-order transition and confirms the long-term colloidal stability of the ferrofluids, even after exposure to an external DC magnetic field. Such long-term colloidal stability is immensely important for practical applications for predictable and reproducible thermal doses to cancerous tissues.

Figure 1d shows a bar chart comparing the SAR values of the oriented and random ferrofluids during RFAMF exposure under three different field amplitudes. In the present study, the highest SAR values were $\sim 291.2 \pm 9.8$ and 179.9 ± 6.6 W/g_{Fe} for the oriented and random samples, respectively, with MNP concentration of 6 wt. %, under a RFAMF amplitude of 33.1 kA/m, indicating a SAR enhancement of ~ 62 % after *in-situ* orientation. During the course of the experiment, the MNP concentrations, exposure time, RFAMF amplitude and frequency were kept constant and this significant enhancement in SAR was solely attributed to an enhancement in anisotropy energy density along the chain direction, as discussed below.

In the presence of an external DC magnetic field (H_{DC}), the SPM MNPs acquire a dipolar moment and experience an attractive interaction along the direction of H_{DC} . This leads to the formation of linear chain-like structures, due to head-on aggregation along the

direction of H_{DC} . Formation of such linear chain-like structures was experimentally verified using optical phase contrast microscopy and AFM imaging. Figures 2a-b show the optical phase contrast microscopy images for the ferrofluids with MNP concentrations of 3 and 6 wt. %, respectively. The presence of linear chain like structures along the direction of H_{DC} is clearly evident from the figures. It was further observed that the chain lengths increased with MNP concentration. Figure 2c shows a typical AFM topography image of the oriented ferrofluid, obtained by drop casting a diluted (0.01 wt. %) sample on a freshly cleaved mica substrate and dried in-situ under $H_{DC} \sim 80$ G. The presence of linear chain-like structure, consisting of the SPM MNPs, is clearly evident from the AFM topography image. Figure 2d shows the 3D topography of Figure 2c, where the presence of the SPM MNPs, along the chains, is clearly discernible. The typical topographic heights of the chain forming units were ~ 7 -10 nm, confirming that the chains were indeed formed by the oriented MNPs.

Following the Stoner-Wohlfarth model, the energy (E_s) of a single MNP, exposed to a H_{DC} , is expressed by the following equation.

$$E_s = -K_{eff}V_p \sin^2 \theta - \mu_0 M_s H_{DC} \cos(\theta - \phi) \quad (2)$$

Here, θ is the angle between the H_{DC} and magnetization and ϕ is the angle between the H_{DC} and the RFAMF. For an assembly of MNPs oriented parallel to H_{DC} , the total energy of the chain (E_c), consisting of Q number of MNPs, is expressed by the following equation.

$$E_c = - \left[\frac{3V_p^2 M_s^2}{(D_p + D_{s-s})^3} \sum_{i=1}^Q \frac{Q-1}{Q^i} + K_{eff} V_p \right] \sin^2 \theta - \mu_0 M_s H_{DC} \cos(\theta - \phi) \quad (3)$$

Here, the first term represents the dipole-dipole interactions between the MNPs in a chain and the second term indicates the effective anisotropy of individual MNPs. D_p and D_{s-s} indicate the MNP diameter and surface to-surface separation between the neighboring MNPs, within a chain, respectively. For $Q=1$, E_c reduces to E_s . Figure 3a shows the variation of the anisotropy energy barrier for H_{DC}



Figure 2: Optical phase contrast microscopy images showing linear chain-like structures along the direction of an external magnetic field ($H_{DC} \sim 80$ G, indicated in the figure) for ferrofluids with MNP concentrations of (a) 3 wt. % and (b) 6 wt. %. (c) AFM topography image of oriented ferrofluid (serially diluted) dried in-situ on a freshly cleaved mica substrate, in the presence of $H_{DC} \sim 80$ G. (d) 3D topography view of Figure 2c

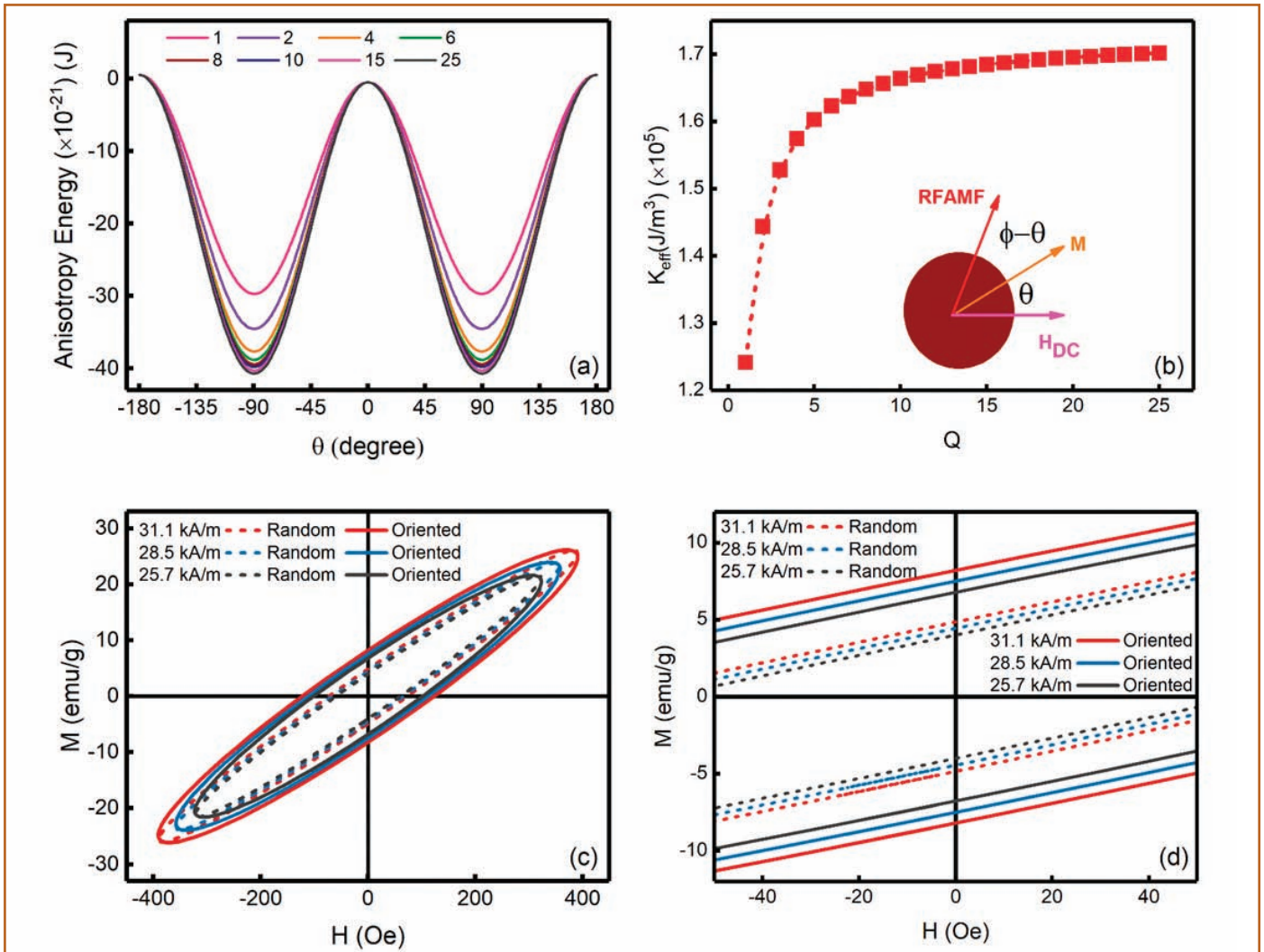


Figure 3: (a) Variation of anisotropy energy barrier for H_{DC} induced chains with varying numbers ($= Q$) of MNPs, as a function of θ . (b) Variation of K_{eff} as a function of Q . (Inset) Geometry of H_{DC} , M and RFAMF . (c) Dynamic hysteresis loops for the oriented (solid lines) and random (dashed lines) samples, subjected to three different RFAMF amplitudes at a RFAMF frequency of 126 kHz. (d) Magnified view of Figure 3c in the low field region

induced chains with varying numbers of MNPs, as a function of θ ($\phi = 0$, as H_{DC} is set parallel to RFAMF).

It can be seen from Figure 3a that the energy landscape shows two stable minima at $\pm 90^\circ$, corresponding to the up and down directions of the magnetic moments. It was further observed that the anisotropy barrier height increased asymptotically with increasing Q , indicating an enhancement in anisotropy energy density along the direction of H_{DC} , as a function of Q . Figure 3b shows the variation of effective anisotropy energy density (K_{eff}) as a function of Q . It is evident from the Figure 3b that the enhancement in anisotropy energy density was significantly higher for chains consisting of a few MNPs and for larger chains, anisotropy energy

density exhibited saturation. The average chain length $\langle Q \rangle$ was estimated under the auspices of de Gennes' flexible chain model. According to this model the MNP chains are flexible in nature and $\langle Q \rangle$ represents the rigid unit, which is analogous to the Kuhn length of polymer. Larger chains are formed due to orderly longitudinal aggregation among the Kuhn units along the direction of H_{DC} . In the low field limit ($\alpha = \frac{mH_{\text{DC}}}{k_B T} < \gamma = \frac{m^2}{d^3 k_B T} > 1$, in the present case $\alpha = 0.3$ and $\gamma = 2.78$) the estimated $\langle Q \rangle$ values were 2.33, 2.56, 2.79 and 3.02 for ferrofluids of concentration 3, 4, 5 and 6 wt.% respectively. The effective anisotropy energy density values, for various $\langle Q \rangle$, were estimated from the calibration curve (Figure 3b), which were then utilized further to probe the role of chain formation on SAR enhancement.

To theoretically probe the effect of H_{DC} induced chain formation on RFAMF induced heating efficiency of the oriented as well as the random samples, dynamic hysteresis loop simulations were carried out using the AC magnetic field: $H(t) = H_{max} \cos(\omega t)$ and magnetization: $M(t) = |\chi| H_{max} \cos(\omega t + \delta)$.

Here, the phase lag (δ) in $M(t)$ is due to the time delay in magnetization switching following the rapidly (~ 126 kHz) oscillating $H(t)$ and is expressed as $\delta = \tan^{-1}(\omega\tau)$. $|\chi|$ indicate the modulus of the complex ferrofluid susceptibility and is expressed as $|\chi| = \chi_0 / \sqrt{1 + \omega^2 \tau^2}$, where considering uniaxial anisotropy, χ_0 is expressed as by the following equation.

$$\chi_0 = \chi_{DC} \left[\frac{3e^\sigma}{\sqrt{\pi\sigma} \operatorname{erfi}(\sqrt{\sigma})} - \frac{3}{2\sigma} \right] \quad (4)$$

Here, $\sigma = K_{eff} V_p / k_B T$, $\chi_{DC} = \mu_0 M_s^2 / 3k_B T$, and $\operatorname{erfi}(\sigma) = \left(\frac{2}{\sqrt{\pi}} \right) \int_0^{\sqrt{\sigma}} e^{x^2} dx$.

Figure 3c shows the dynamic hysteresis loops (at 126 kHz) for the oriented and random samples, subjected to RFAMF amplitudes of 31.1, 28.5 and 25.7 kA/m. Figure 3d shows the magnified view of Figure 3c in the low field region. It is evident from Figures 3c-d that for a fixed RFAMF amplitude, the loop area (A) was significantly larger for the oriented samples, indicating a higher SAR (as $SAR \sim A \cdot f$). For the oriented samples, the phase lag (δ) in $M(t)$ increased due to an enhancement in anisotropy energy density, resulting in higher dynamic coercivity during field switching. This resulted in a larger loop area (and SAR) for the oriented samples, which is in good agreement with the experimental temperature rise curves. In the present study, $\sim 62\%$ enhancement in the SAR was obtained for the oriented samples (at 6 wt. % for RFAMF amplitude of 33.1 kA/m). The maximum theoretical enhancement in SAR was found to be $\sim 68\%$ and the slight mismatch with the experimental value was attributed to various factors such as size polydispersity, chain-chain interactions and distributions in chain density.

Further, to probe the bio-compatibility of the phosphate coated Fe_3O_4 MNPs, cytotoxicity studies were carried out using human lung epithelial cell line (L132) following the standard MTT assay protocol and Figure 4a shows the cell viability after 24 hours of incubation as a function of sample concentration. The phosphate coated Fe_3O_4 MNPs showed significant biocompatibility up to 6.25 $\mu\text{g/mL}$, which indicated the suitability of this sample for practical applications. Figs. 4b-c show the optical phase contrast

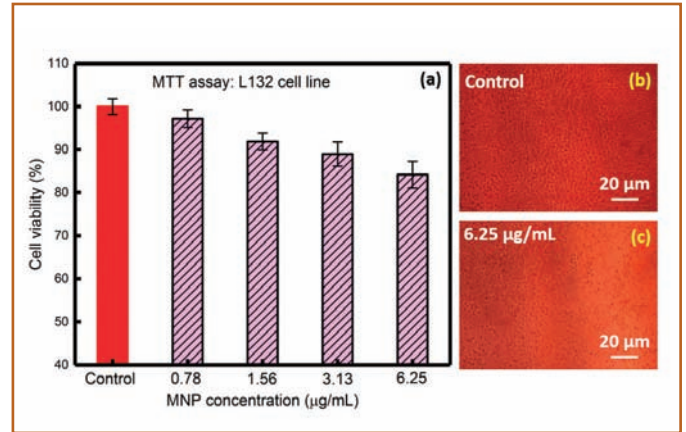


Figure 4: (a) Cell viability (in %) as a function of MNP concentration for the phosphate coated Fe_3O_4 MNPs. Optical phase contrast microscopy images of (b) control and (c) cell line loaded with 6.25 $\mu\text{g/mL}$ MNP

microscopy images of the control and cell line loaded with 6.25 $\mu\text{g/mL}$ of MNPs respectively, where the viable cells are clearly visible.

The proposed *in-situ* orientation method for enhancing heating efficiency, was verified for another aqueous ferrofluid containing tetramethyl ammonium hydroxide coated SPM Fe_3O_4 MNPs of similar crystallite size ($\sim 8.8 \pm 0.9$ nm) but significantly lower anisotropy energy density (~ 75.4 kJ/m³, i.e. 39 % lower) and saturation magnetization (~ 38 emu/g, i.e. 27 % lower). It was observed that external DC magnetic field induced orientational ordering resulted in $\sim 36\%$ enhancement in SAR for this system (MNP concentration ~ 8 wt. %). Dynamic hysteresis loop based theoretical simulations indicated an enhancement in SAR of $\sim 37\%$, which was in agreement with the experimental findings.

In summary, a $\sim 62\%$ enhancement in the specific absorption rate is achieved in a biocompatible aqueous ferrofluid, containing superparamagnetic nanoparticles, through *in-situ* orientation of particles under a static magnetic field. The enhancement in SAR was theoretically understood from dynamic hysteresis loop simulations, without assuming blocked state conditions. The advantage of the proposed H_{DC} induced *in-situ* orientation technique is that it could be coupled with magnetic resonance imaging (MRI) instrument. Additionally, the proposed technique also opens up the possibility of synergistically using MRI-based diagnostic along with MFH-based therapeutics toward development of an efficient theranostic methodology. The observed SAR enhancement offers possibilities of reducing the exposure time during therapy and provides further impetus towards the realization of MFH as an effective cancer therapeutic procedure.

Training programme

About BITS Summer Practice School at IGCAR

June 26, 2020

Forty Nine students from BITS Pilani, Hyderabad and Goa Campuses pursuing degrees in various disciplines like Mechanical, Chemical, Civil, Electrical & Electronics. Electronics & Instrumentation, Electronics & Communication, Computer Science and B.Ss. / M.Sc. Physics underwent summer practice school during May 22 to June 26, 2020 through virtual mode using video conference facilities. Dr. Sanket Goel and Dr. Sandip Deshmukh from Hyderabad campus were the program coordinators from BITS. Dr. Arun Kumar Bhaduri, Distinguished Scientist and Director, IGCAR & GSO inaugurated the practice school programme via online and interacted with the students on May 22, 2020. Dr. B. Venkatraman, Director, SQRMG and ESG delivered an orientation lecture to all the students on "Non-destructive evaluation and its role" including details about the R&D at IGCAR on May 28, 2020. The students carried out challenging projects through interaction with enthusiastic faculty at IGCAR and their expert guidance. Bi-weekly review system with one to one interaction between student and faculty along with coordinators from BITS and IGCAR ensured proper imparting of knowledge to the students without compromising the quality in this new methodology of interactions this year. The final project work presentations, group discussions and viva-voce were all conducted successfully in the remote mode. The programme successfully concluded on June 26, 2020 and the certificates have been dispatched by post to the students.

*Reported by
Organising Team, BITS-Practice School*

News and Events

6th International Day of Yoga

June 21, 2020

The sixth International Day of Yoga was observed on June 21, 2020 at IGCAR, Kalpakkam through an online programme. A demonstration of yoga practices in the morning followed by a special lecture of Sr. Prof. K. R. Munirathinam, Sky Yoga, Chennai was arranged. Many employees of IGCAR and other DAE Units at Kalpakkam participated in the programme and were benefitted by it.

*Reported by
Shri O. T. G. Nair, Director (P&A)*

Measures related to COVID-19 at IGCAR

As part of measures to control and combat COVID 19, planning and implementation of sanitisation and other precautionary/preventive measures were carried out at Kalpakkam complex. Further, few models of dispensers of hand sanitisers were developed and installed at different buildings.

I. Precautionary/preventive measures

- Thermal Screening of all the employees was done (by Health, Safety & Environment Group) at the Main Gate and at the entrance inside IGCAR-BARC(F) Gate and at FRFCF Gate.
- Sanitisation of:
 - ▶ All the public places of Kalpakkam and Anupuram Townships.

- ▶ Departmental buses and light vehicles and private vehicles of employees.
- ▶ Turnstile Gates at the Main, IGCAR-BARC(F), and Kokilamedu entry points. This was carried out in coordination with fire station.
- ▶ Building entrances, Control Rooms and all common access area in the Reactor Complex and Plants, Laboratories, Occupational Health Centres, Health physics and safety laboratories etc.
- ▶ Vehicles bringing consignment to IGCAR campus.
- Marking the social distancing square in common area and fixing sanitiser dispensers in all important locations inside IGCAR complex.
- Sign boards were fixed at barricades at IGCAR main gate.
- Procurement and distribution of sanitising items, masks, PPE's.
- Automatic hand sanitisers were procured and installed at entry points in main buildings and security complex and refilling done periodically.
- Volunteers were engaged for sanitisation & for ensuring social distancing of employees and contract workers at bus alighting points and other places.
- Four labour colonies with around 2500 migrant workers of major contractors of FRFCF were closely monitored during COVID-19 lock-down ensuring COVID-19 ration & sanitisation and proactively mitigating unrest through motivational talks involving district police and administrative authorities. Their travel to native places was arranged batch wise and required transport arrangements were made.
- Special provisions were made at Lunch rooms for ensuring social distancing during dining.
- The access to lunch room (Reprocessing Group) was restricted by installing RFID based biometrics access control system and the seating was arranged through appropriate immobilization of the seats.
- Video conferencing facilities were enabled with the help of Electronics and Instrumentation Group. Secure desktop video Conferencing (IGCAR Vi-Meet) and File-share services were implemented in Internet for IGCAR & other DAE units at Kalpakkam; This enabled organizing virtual meetings for official discussions, technical meetings, PhD review meetings/viva voce, pre-despatch remote inspections with officials Working From Home (WFH) and vendors.
- Remote access to all e-journals were enabled for the benefit of officials and research scholars WFH by SIRD, SQRMG



Thermal Screening in Bus



Thermal Screening of Employees Travelling by Vehicles



Thermal Screening at IGCAR Gate



Sanitisation Measures at a) FBTR, b) Fire Station c) Central Cafeteria and d) Occupational Health Centre



Sanitisation of Bus



Hand Sanitiser Dispenser at IGCAR Gate



Sanitisation of Buildings



Pep Talk with Workers at FRFCF Site

II. Products Developed

Different models of dispenser of hand sanitisers were developed at IGCAR. Following are the details.

Model	Located at
Wall mountable model (Figure 1) Portable unit (Figure 2a) (based on retractable sliding mechanism)	Different locations in FBTR
Foot operated Dispenser (Figure 2b) (Based on link mechanism)	Different places in Materials Chemistry & Metal Fuel Cycle Group (MC&MFCG), Civil engineering Division and Non Destructive Evaluation division.
Manual Dispenser (Figure 2c)	Different places in Reprocessing Group (RpG), GSO and Autoshop
Foot operated Hand Wash station with provision for running water, hand wash soap solution and hand sanitiser (Figure 3)	At MC&MFCG
Auto hand sanitizer dispenser based on using IR sensor with solenoid valve (Figure 4)	

Hand Sanitiser liquid: About 600 liters of hand sanitizer liquid (Figure 5) consisting of isopropanol, hydrogen peroxide, glycerol and water is being prepared every month (by MC&MFCG and HS&EG) and colouring using permitted food colours was ensured to differentiate it from water. The hand sanitisers are being distributed regularly to various facilities at Kalpak-kam



Figure 1: Wall Mountable Sanitiser at FBTR



Figure 3: Foot Operated Hand Wash Station



Figure 4: Auto Hand Sanitiser



(a)



(b)



(c)

Figure 2: Foot Operated Sanitiser installed at various locations (a) FBTR (b) MC&MFCG and (c) RpG

HBNI-IGCAR Corner

Ph.D Thesis Defense

Name	Title	Date	Discipline
Ms. Vinita Daiya	Wirelessly Powered Secured Backscatter Communication for Wireless Sensor Network	20.05.2020	Engineering Sciences
Shri K. Natesan	Development of Mathematical Models and Investigation of FBR Plant behaviour during transients by a Coupled Single and Multi-Dimensional Approach	21.05.2020	Engineering Sciences
Shri P. A. Manojkumar	Synthesis and Modification of Graphene Nanowalls using Plasma Immersion Ion Implantation and Deposition Facility	17.06.2020	Engineering Sciences
Ms. Revati Rani	Tribological properties of ultrananocrystalline diamond films at high temperature and controlled atmosphere	29.06.2020	Physical Sciences

Awards and Honours

Dr. Arup Dasgupta, PMD, MCG/ MMG has been appointed as **Managing Editor**, Transactions of Indian Institute of Metals, Kolkata.

Biodiversity Basket - Avian Fauna

Black Drongo



Photographed by SIRD

Black Drongo is a slim, glossy black bird with a long and deeply forked tail. It has very a small white spot near to the base of its bill and this helps to identify black drongo from other drongos. They mainly feed on insects and sometimes smaller birds. They attack much larger species that approach their nesting territory. This behaviour led to their former name “King Crow”.

Editorial Committee Members: Dr. T. S. Lakshmi Narasimhan, Dr. N. V. Chandra Shekar, Ms. S. Rajeswari, Dr. John Philip, Dr. V. S. Srinivasan Dr. C. V. S. Brahmananda Rao, Shri A. Suriyanarayanan, Shri M. S. Bhagat, Shri G. Venkat Kishore, Dr. Girija Suresh, Shri M. Rajendra Kumar, Shri S. Kishore, Ms. R. Preetha, Dr. N. Desigan, and Shri K. Varathan.